Time-dependent changes in failure stress following thrust earthquakes

Andrew M. Freed[1]

Department of Geosciences, University of Arizona, Tucson

Jian Lin

Department of Geology and Geophysics, Woods Hole Oceanographic Institution, Woods Hole, Massachusetts

Abstract. Two-dimensional (2-D) viscoelastic finite element models were used to calculate the time-dependent changes in Coulomb failure stresses following thrust earthquakes due to respective effects of relaxation of viscous lower crust or upper mantle and postseismic creep on the main fault or its downdip extension. Results suggest that thrust earthquakes cause a coseismic increase in Coulomb stress along antithetic lobes normal to the slip plane. Following a quake, creep processes that reduce stresses in a ductile lower crust or upper mantle are calculated to cause a transfer of stress to the upper crust. Under certain conditions, transfer of stress may lead to a further buildup of high Coulomb stress along the base of the upper crust, potentially shortening the time to failure of other faults in the region. The conditions under which an antithetic lobe of high Coulomb stress are favored to expand at the base of the upper crust postseismically within a few decades include the following: the lower crust or upper mantle has an effective viscosity not greater than 10^{19} Pa s; the thrust fault has a moderate dip angle (40°-50°); the brittle/ductile transition is deep enough to provide a corridor at the base of the upper crust for expansion; and the crust has a low apparent coefficient of friction (<0.2). Postseismic increases in Coulomb stress within the upper crust may also be caused by aseismic creep on the fault. Stress changes due to this mechanism are maximized with a high apparent coefficient of friction. Analysis of experimentally determined non-Newtonian flow laws suggests that wet granitic, quartz, and feldspar aggregates may have a viscosity of the order of 10^{19} Pa s. The calculated rate of stress transfer from a viscous lower crust or upper mantle to the upper crust becomes faster with increasing values of the power law exponent and the presence of a regional compressive strain rate. Results of this 2-D analysis suggest a potentially important role of viscous flow in controlling time-dependent postseismic stress changes that warrant further investigation using 3-D viscoelastic analysis.

1. Introduction

Thrust faulting earthquakes pose substantial seismic hazard in many parts of the world including southern California. For example, the 1971 M_w=6.7 San Fernando quake occurred on surface-cutting faults beneath the San Gabriel Mountains north of the Los Angeles Basin (Figure 1). Only 23 years later the 1994 M_w=6.7 Northridge quake occurred on a blind thrust fault beneath the San Fernando Valley about 30 km to the southwest. Both of these events may have resulted from convergence between the "big bend" of the San Andreas fault north of the San Gabriel Mountains and motion of the Pacific plate [*Wentworth and Yerkes*, 1971]. While both quakes are likely a response to a common cause of high stress state of the region, the observed overlap between their aftershock zones (Figure 1) and the relatively short time interval between them lead to the hypothesis that the two quakes might be linked

through stress interaction [*Stein et al.*, 1994; *Mori et al.*, 1995]. This points to an interesting possibility that stress changes caused by a moderate event on a thrust fault may advance (or delay) the occurrence of future quakes on adjacent thrust faults.

Most current studies of earthquake stress interactions have focused on coseismic stress changes immediately following an earthquake. However, observational evidence suggests that strain rates in southern California may change significantly on timescales of years to decades following a quake. For example, recent geodetic studies of *Shen et al.* [1996a] have revealed that strain rates in southern California appear to mimic the pattern of historic seismicity, suggesting that either earthquakes occur at regions of high strain rates or that postseismic deformations are significant and long lasting or both. In addition, well-monitored postseismic deformation following the 1983 M_w=6.5 Coalinga [*Stein and Ekstrom*, 1992], the 1992 M_w=7.3 Landers [*Shen et al.*, 1994; *Wyatt et al.*, 1994; *Bodin and Gomberg*, 1994], and the 1994 Northridge [*Donnellan and Lyzenga*, 1996], California, quakes suggests that creep mechanisms in the crust respond rapidly (months) to stress changes imposed by earthquakes. Generally, two mechanisms are considered in explaining observed postseismic surface deformation: further slip on the fault plane [*Thatcher and Rundle*, 1984; *Tse and Rice*, 1986] and
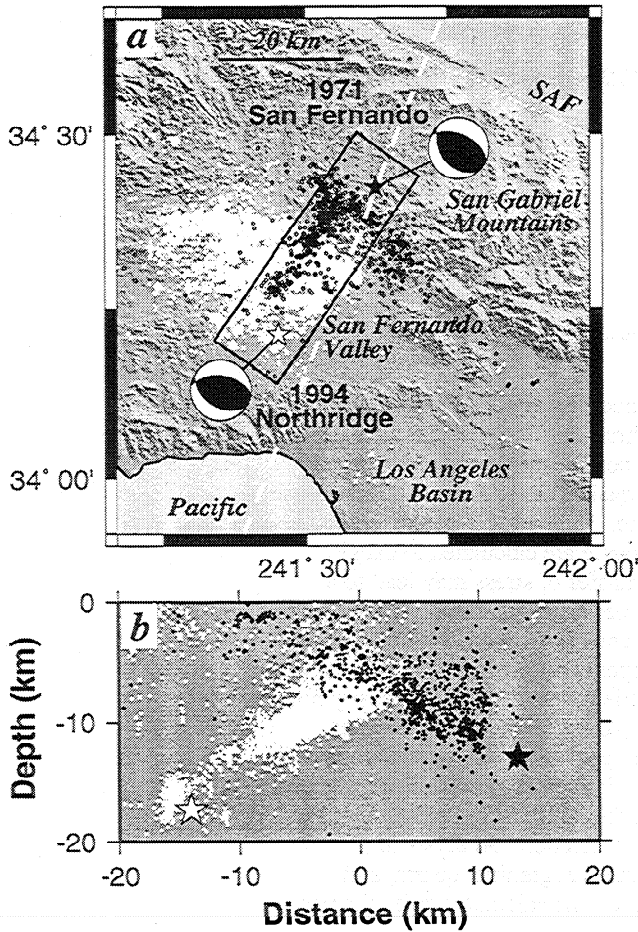
Figure 1. Focal mechanisms and aftershocks [*Mori et al.*, 1995] associated with the 1971 San Fernando and 1994 Northridge, California, earthquakes: (a) map view and (b) depth cross section. The rectangle in the map view encloses the events plotted in the cross section. Dashed white line shows the two-dimensional cross section considered in the finite element analysis of the San Fernando quake. The orientation of the cross section is based on a regional stress direction of N16°E [*Stein et al.*, 1994].

viscoelastic relaxation of the lower crust and/or upper mantle [*Nur and Mavko*, 1974; *Thatcher and Rundle*, 1984; *Li and Rice*, 1987]. If postseismic surface deformation is caused by further slip of the fault, the corresponding postseismic Coulomb stress changes should have a similar distribution as that suggested by the coseismic calculation, while magnitude will increase proportionally to the increase in slip. However, if postseismic surface deformation is caused by relaxation of a ductile lower crust or upper mantle, postseismic Coulomb stress changes may vary in distribution and increase significantly in certain locations as more coseismic load is transferred to the brittle upper crust with time.

In this study we investigate the two-dimensional (2-D) characteristics of postseismic stress changes following thrust earthquakes with particular focus on their dependence on such important parameters as fault geometry, crustal rock rheology, and whether the faults are surface-cutting or deeply buried (blind). Because the along-strike lengths of many interplate faults tend to be of similar magnitude to their downdip lengths, earthquake stress changes tend to vary in three dimensions. In such cases the 2-D assumption is reasonable only near the perpendicular bisector of the fault. For this reason the present

study should be viewed as a prediction of how crustal relaxation influences stresses along the modeled cross section, but results should not be extrapolated off axis. The Northridge quake was located ~15 km off axis from the San Fernando quake. Future time-dependent 3-D studies are required to understand off-axis stress relationships of short faults. However, as an initial step, we illustrate results of 2-D modeling calculations on two distinct examples of thrust faults: a shallow dipping, blind thrust fault with relatively short downdip length, which represents the 1983 Coalinga, California, quake and a steep, surface-cutting thrust fault with a long downdip length, which is typified by the 1971 San Fernando event. Results of 2-D analyses suggest a potentially important role of viscous flow in lower crust and upper mantle in controlling time-dependent postseismic stress changes.

2. Modeling Approach

Analyses were conducted using TECTON 2-D plane-strain, finite element models [*Melosh and Raefsky*, 1980]. Comparisons between 2-D and 3-D elastic results suggest that the 2-D assumption is reasonable along the perpendicular bisector of a short fault as illustrated later in section 4. Earthquakes are simulated by applying a seismically inferred slip distribution to a predetermined fault plane using split nodes [*Melosh and Williams*, 1989]. Coseismic stresses are calculated based on deformations in the crust caused by this slip. Postseismic stresses are then calculated by allowing ductile regions of the crust to relax with time. We utilize both Newtonian and non-Newtonian flow laws to describe the viscous relaxation.

One of the more widely used criteria to characterize the conditions under which rock failure occurs is Coulomb failure [*Jaeger and Cook*, 1979]. The calculation is based on the geometry and slip of the earthquake, the sense of orientation of faults in the surrounding crust, and the apparent coefficient of friction [e.g., *King et al.*, 1994]. The usefulness of Coulomb stress calculations to predict regions of subsequent failure has been supported by reasonable agreement between regions of predicted coseismic Coulomb stress increases and the locations of aftershocks and has become a common approach to earthquake triggering analyses [e.g., *Oppenheimer et al.*, 1988; *Reasenberg and Simpson*, 1992; *Stein et al.*, 1992; *Harris and Simpson*, 1992; *Jaume and Sykes*, 1992; *King et al.*, 1994; *Stein et al.*, 1994; *Simpson and Reasenberg*, 1994].

Coulomb stress changes are calculated based on the Coulomb failure criterion where failure occurs on a plane when the change in Coulomb stress $\Delta\sigma_c$ exceeds a specific value,

$$\Delta\sigma_c = \Delta\tau - \mu' \Delta\sigma_n \qquad (1)$$

where $\Delta\tau$ is the change in shear stress on the failure plane, $\Delta\sigma_n$ is the change in the total confining pressure resulting from the difference between the normal stress and the pore fluid pressure, and μ' is the apparent coefficient of friction. We use the term "apparent" to describe the coefficient of friction because the level of pore pressure, which has a significant influence on the confining pressure, is poorly known in the southern California crust.

The Coulomb stress calculation used in the present analysis considers the component of earthquake-induced stresses in the direction of optimally oriented secondary fault planes θ, given by

$$\theta = \phi + \beta \qquad (2)$$

where ϕ is a function of the stress field (regional and coseismic),

$$\phi = 0.5 \tan^{-1}[2\sigma_{xy} / (\sigma_x - \sigma_y)] \qquad (3)$$

where σ_{xy} is the absolute shear stress, and σ_x and σ_y are the absolute normal stresses; β is a function of the apparent coefficient of friction μ',

$$\beta = 0.5 \tan^{-1}(1/\mu') \qquad (4)$$

If the orientation of a specific secondary fault is known, that orientation can be used. In most cases, however, the location and geometry of secondary faults are not known and thus must be assumed. Since regional normal stresses are generally considered to be much larger than coseismic stresses, ϕ tends to be controlled by the regional stress field. In a 2-D analysis the regional stress field is assumed to be oriented in line with the plane modeled. We assumed a regional lateral compressional stress of 10 MPa. The finite element method for calculating Coulomb stress changes was tested by comparing results to identical dip-slip boundary element models. Results showed that the two methods produced identical 2-D elastic results.
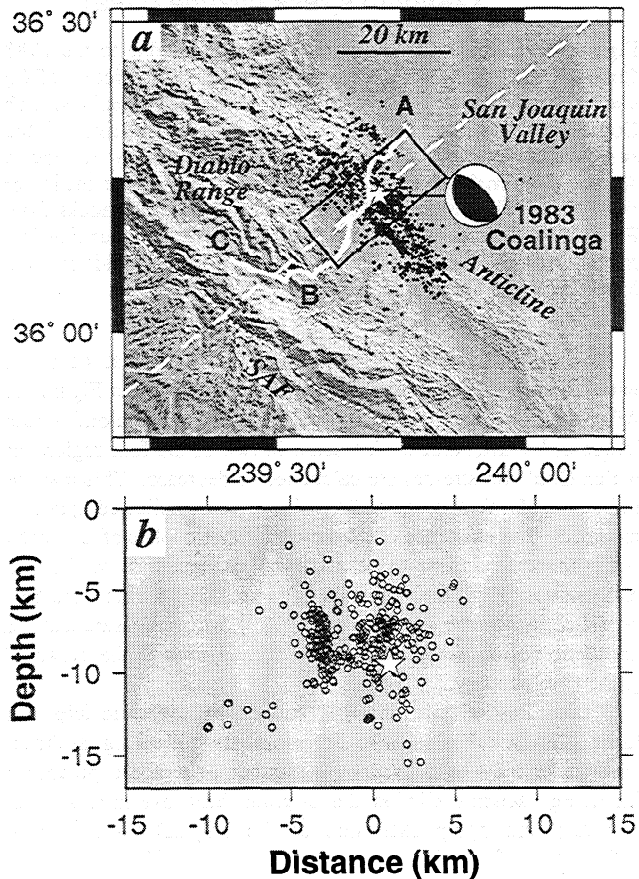

Figure 3. (a) Central portion of the two-dimensional (2-D) finite element model used to study the 1983 Coalinga earthquake. The full model is 150 km wide and 60 km deep. This cross section is shown in Figure 2 as a dashed white line. Layer numbers correspond to material properties listed in Table 1. The fault length is 4 km (white line with arrows), and the slip distribution is assumed to be parabolic with no slip at the ends and 4.7 m of slip in the middle [*Stein and Ekstrom*, 1992]. Thin lines that extend the fault plane show the modified fault lengths (2 km to either the updip or downdip directions). (b) Comparison of observed (circles) [*Stein and Ekstrom*, 1992] and calculated (curve) coseismic surface elevation changes caused by the 1983 Coalinga earthquake. Observed data have been corrected for leveling errors and nontectonic subsidence [*Stein and Ekstrom*, 1992].

3. Results

3.1. Blind Thrust Fault: 1983 Coalinga Quake

3.1.1. Model assumptions. The May 2, 1983, M_w=6.5 Coalinga, California, earthquake, which occurred 35 km northeast of the San Andreas fault and 16 km north of the town of Coalinga (Figure 2), was chosen as a case study of a blind thrust fault. The rupture occurred along a blind thrust beneath the Coalinga anticline, which is the northwest segment of a 110-km-long zone of anticlines near the boundary between the San Joaquin Valley and the southeastern Diablo Range of the central California Coast Ranges [*Stein and Ekstrom*, 1992]. The Coast Ranges are a product of the oblique convergence of the North American and Pacific plates. The 2-D model of the Coalinga region considers a southwest-northeast cross section perpendicular to the San Andreas fault as shown by the white dashed line in Figure 2. The inner portion of the finite element mesh is shown in Figure 3a. The mesh is 150 km long normal to the fault and extends to a depth of 60 km. The bottom boundary is fixed in both vertical and horizontal directions, and the side boundaries are fixed in the horizontal direction. Our analysis has determined that specific choices for these boundary conditions do not significantly influence model results. The Coalinga slip plane

Figure 2. Focal mechanism and aftershocks associated with the 1983 Coalinga, California, earthquake at the edge of the Diablo Range and San Joaquin Valley: (a) map view and (b) depth cross section [*Ekstrom et al.*, 1992]. The rectangle in the map view encloses the events plotted in the cross section. Dashed white line shows the two-dimensional cross section (N50°E) considered in the finite element analysis. Solid white line (A-B-C) shows the routes of the leveling surveys used in coseismic and postseismic surface deformation measurements. Dotted line shows the San Andreas fault (SAF).
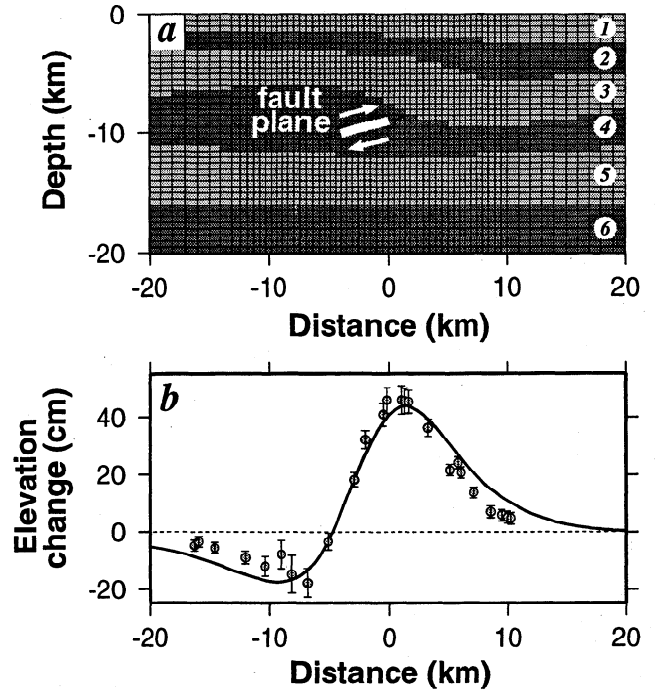
(Figure 3a) is modeled after *Stein and Ekstrom* [1992], who suggested that the seismicity and geodetic data of Coalinga can best be explained by a shallow (15°) southwest dipping thrust fault. The fault has an approximate downdip length of 4 km and an along-strike length of 20 km [*Stein and Ekstrom*, 1992].

The stratigraphy of the Coalinga area consists of a thick sequence of Cretaceous through Quaternary strata of the Great Valley Sequence and the Franciscan Assemblage [*Page*, 1981]. Beneath the Franciscan Assemblage, at a depth of about 15 km, the basement beneath Coalinga has been inferred to be a slab of ophiolite that was obducted onto the continental margin during Jurassic time [*Hopson et al.*, 1981]. The Moho discontinuity beneath the western San Joaquin Valley is estimated to be at a depth of about 25 km [*Fuis and Mooney*, 1990]. Stratigraphic layers, differentiated by changes in shading in Figure 3a, are modeled as units of constant elastic properties. Density values were based on seismic reflection experiments and gravity modeling [*Griscom and Jachens*, 1990]. Young's modulus is based on P wave velocities from the three-dimensional inversion study of *Eberhart-Phillips* [1990] and the relationship

$$E = (2/3) (1+v) \rho V_p^2 \qquad (5)$$

where E is Young's modulus, v is Poisson's ratio, ρ is density, and V_p is P wave velocity. Table 1 lists the elastic properties used in the modeling of the Coalinga earthquake.

3.1.2. Coseismic Changes. We modeled the slip distribution on the Coalinga fault plane as parabolic, with a maximum displacement of 4.7 m in the middle of the fault plane that tapers to zero at the fault top and bottom [*Stein and Ekstrom*, 1992]. This model reproduces reasonably well the observed coseismic surface elevation changes (Figure 3b). The measured elevation changes are based on data from a leveling survey (see line A-B in Figure 2) that has been projected onto the cross section of the model. The measurements have been corrected for leveling errors and nontectonic subsidence [*Stein and Ekstrom*, 1992].

Coseismic Coulomb stress changes caused by the Coalinga earthquake, calculated based on assumed apparent coefficients of friction of μ'=0.0 and μ'=0.6, are shown in Figures 4a and 4b, respectively. The main feature of the stress distribution is four lobes of high Coulomb stress increase (white regions). Two of these lobes are located at the top and bottom ends of the fault plane and are caused by the high shear stresses associated with slip termination. The other two lobes are oriented antithetically to the fault plane and are caused by bending of the crust associated with fault slip. The higher coefficient of friction (Figure 4b) increases stress magnitudes in the lower crust but has only a minor influence on the magnitude of stresses in the upper crust. The higher friction coefficient also leads to shallower dips of the calculated optimally oriented slip planes as shown in the bottom right-hand corner of Figures 4a and 4b.

Table 1. Elastic Properties for the Coalinga Model

Layer*	V_p, km s^{-1}	ρ, kg m^{-3}	E, MPa	v
1	3.0	2250	1.6×10^4	0.25
2	4.0	2400	3.2×10^4	0.25
3	5.0	2600	5.4×10^4	0.25
4	5.7	2700	7.4×10^4	0.25
5	6.3	2900	9.5×10^4	0.25
6 (15-25 km)	6.5	3000	1.0×10^5	0.25
7 (25-50 km)	8.0	3250	1.7×10^5	0.25

*Layer numbers correspond to numbers shown in Figure 3a

Value V_p is the P wave velocity; ρ is the density; E is Young's modulus; v is Poisson's ratio.
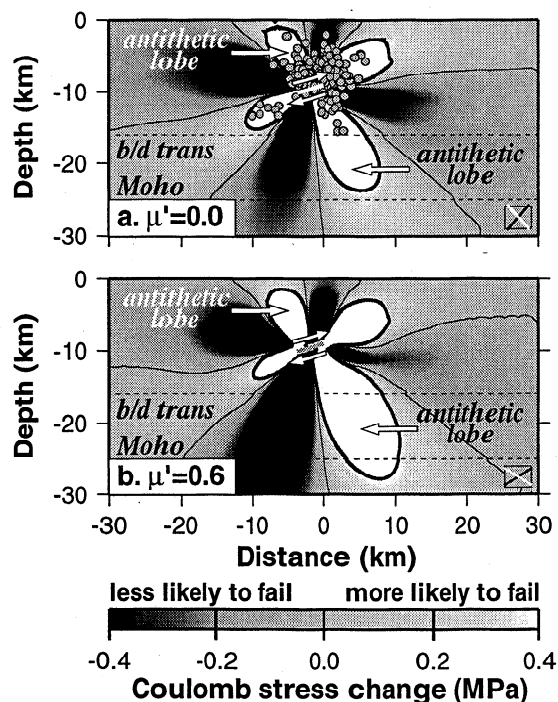

Figure 4. Calculated Coulomb stress changes due to the 1983 Coalinga earthquake for an apparent coefficient of friction of (a) μ'=0.0 and (b) μ'=0.6. White regions are areas of calculated high Coulomb stress increases, where subsequent faulting of the surrounding rock is predicted to be more likely to occur. Assumed optimal slip planes are shown in the boxes at the lower right corner of each plot. Shaded circles are the aftershocks from Figure 2b. Bold contour line is 0.4 MPa. Thin contour line is 0 MPa. Abbreviation b/d trans is brittle/ductile transition, and Moho indicates Moho discontinuity.

Coalinga aftershocks [*Ekstrom et al.*, 1992] that occurred within 5 km of the modeled cross section are plotted in Figure 4a. Aftershocks occur in all four lobes of calculated Coulomb stress increase; but aftershocks also occur in two of the four regions in which Coulomb stresses are calculated to decrease. This may be indicative of a fault plane or fault slip more complicated than that modeled. The existence of predicted antithetic lobes of Coulomb stress increase appear to be a natural consequence of dip-slip earthquakes. High shear stresses in an antithetic region were also predicted by *Melosh and Williams* [1989], who suggested that the antithetic region associated with a normal fault is the cause of graben morphology.

3.1.3. Postseismic changes caused by aseismic slips on fault planes. Postseismic deformations following a thrust earthquake may be caused by a number of tectonic processes including aseismic slip on the original fault, aseismic slip on downdip and updip extension of the original fault, ductile deformation of the viscous lower crust, or relaxation of the upper mantle. We attempt to distinguish between these mechanisms by comparing calculated surface deformations from each model with geodetic measurements following the 1983 Coalinga quake. Geodetic measurements were made along a leveling line (A-B in Figure 2) in June of 1983 (1 month after the quake) and in July 1987 [*Stein and Ekstrom*, 1992]. Elevation changes during this period were corrected for nontectonic subsidence from water and oil extraction [*Stein and Ekstrom*, 1992].

Figure 5a shows the observed postseismic surface elevation changes and the predicted changes by three models that consider aseismic slip on the fault following the 1983 quake. The updip
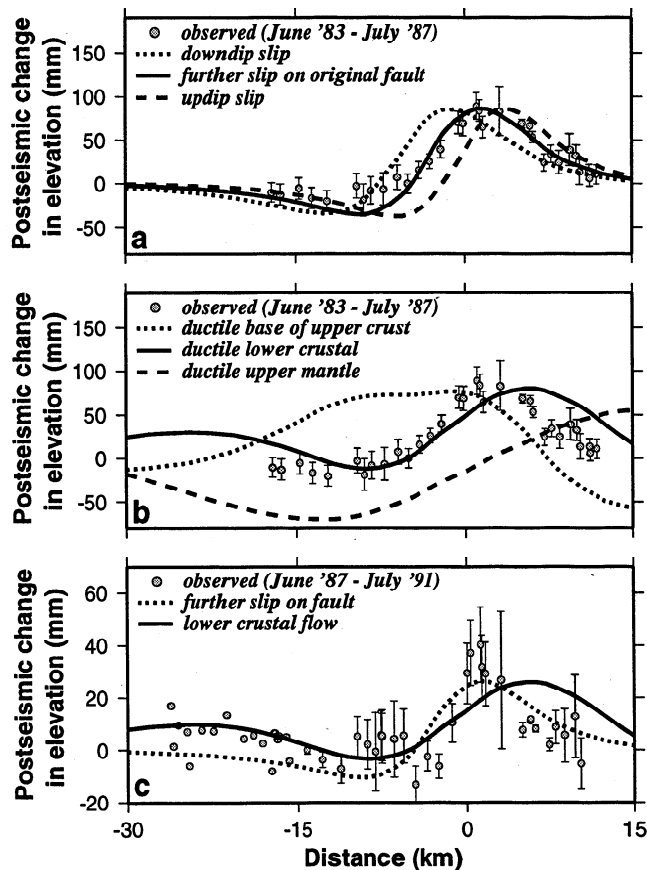
Figure 5. (a) Observed and calculated surface elevation changes from 1983 (after Coalinga quake) to 1987. Calculated results consider models of postseismic aseismic slip on the fault plane (see text). (b) Same observed data as Figure 5a, but calculated results correspond to models of ductile flow (see text). Geodetic data and error estimates in Figures 5a and 5b are from *Stein and Ekstrom* [1992]. (c) Observed and calculated surface elevation changes from 1987 to 1991. Geodetic data in Figure 5c are previously unpublished data from R. Stein (1992). Error bars in Figure 5c represent 50% of the nontectonic subsidence corrections used. Survey errors for Figure 5c are not available.

and downdip models correspond to slip on 2-km extensions of the original fault (thin black lines that extend from the denoted fault in Figure 3a). The amount of slip in each of these models was adjusted such that the amplitudes of the calculated surface elevation changes were approximately the same as those observed. Figure 5a shows that the model with ~0.75 m of postseismic slip on the original fault matches most closely the observed surface elevation changes in the 4 years following the Coalinga quake. These calculations also suggest that models with only updip or downdip postseismic slip do not fit well with the observed postseismic elevation changes. The inference that postseismic deformations in the first few years following the Coalinga quake were caused by creep on the fault was first suggested by *Stein and Ekstrom* [1992]. Creep on the fault plane has also been inferred to be responsible for early postseismic deformations following the 1989 Loma Prieta earthquake [*Burgmann et al.*, 1997] and the 1994 Northridge quake [*Donnellan and Lyzenga*, 1996].

3.1.4. Postseismic changes caused by ductile flows in lower crust. We next considered models in which the crust or upper mantle deform because of ductile processes such as dislocation creep. Aftershock activity following the 1983 Coalinga quake

(Figure 4a) ceases at a depth of about 15 km despite the predicted high calculated Coulomb stress changes below this depth. This could reflect a ductile lower crust that extends down to the Moho (~25 km). Ductile relaxation within the lower crust would lead to a dissipation of lower crustal stiffness with time after the quake. This would have the effect of forcing the upper crust to carry more of the coseismic load, which, in turn, would cause upper crustal deformation to increase beyond that induced by the original fault slip. By assuming a lower crustal viscosity, the finite element model calculates this transient process and predicts changes in deformation and stresses as a function of time after the earthquake.

The amplitude of observed postseismic surface deformation in the 4 years following the Coalinga quake can be approximated by a lower crust with a viscosity of the order of $1x10^{18}$ Pa s (solid line in Figure 5b). The wavelength of the calculated surface deformation, however, is slightly broader than that observed; that is, this model does not provide as good a fit to the observed data as the model that considers further slip on the original fault (solid line in Figure 5a). Furthermore, $1x10^{18}$ Pa s is a relatively low viscosity and it would lead to surface deformations much larger than those observed in the 4- to 8-year period following Coalinga. Thus lower crustal flow is probably not the primary mechanism responsible for surface deformations observed in the first 4 years following the Coalinga quake. This conclusion constrains the viscosity of the lower crust to be higher than $1x10^{18}$ Pa s.

3.1.5. Postseismic changes caused by ductile flows in upper mantle. We also considered the possibility that ductile flow takes place in the uppermost mantle. The Moho is inferred to be at a depth of approximately 25 km below the Coalinga region [*Fuis and Mooney*, 1990]. We calculated the changes in surface elevation based on a model with a mantle viscosity of $1x10^{18}$ Pa s (all other regions are modeled elastically) and compare deformations to those observed in Figure 5b (dashed line). Figure 5b suggests that flow in the mantle following the quake would result in surface deformation much broader than that measured, making it an unlikely candidate to explain the observed surface deformation in the first 4 years after the quake.

3.1.6. Postseismic changes caused by ductile flows in the base of the upper crust. Finally, although there is no evidence to suggest that the lower most portion of the upper crust (layer 5 in Figure 3a) is ductile, we, nevertheless, calculated the surface deformations that would result from ductile flow in this region based on a viscosity of $1x10^{18}$ Pa s. Figure 5b (dotted line) shows that flow in the lower most upper crust would lead to surface elevation changes much different from those observed. Therefore it is also an unlikely candidate to explain the observed postseismic deformation.

The above comparisons between the calculated and observed surface elevation changes in the first 4 years following the Coalinga quake suggest that deformations were most likely caused by further slip on the original fault plane. However, this does not rule out the possibility of a more moderate rate of flow in the lower crust (i.e., associated with a viscosity greater than $1x10^{18}$ Pa s) that may be observable after more postseismic time has elapsed. Another leveling survey was taken in 1991 to measure surface changes in the 4- to 8-year postseismic period, and the leveling line was extended from A-B to A-B-C in Figure 2 [*Stein and Ekstrom*, 1992]. The observed surface deformation between 1987 and 1991 is shown in Figure 5c (note difference in vertical scale from Figures 5a and 5b). Data regarding nontectonic subsidence (water and oil level changes) are not available for this time period. We therefore made the assumption

that the rate of nontectonic subsidence was the same in the period from 1987 to 1991 as that used by *Stein and Ekstrom* [1992] for the period 1983-1987. The error bars in Figure 5c are representative of 50% of this subsidence correction. These error bars do not include potential errors in the geodetic measurements, which are probably of the order of 15 mm based on previous error estimates.

The subsidence corrections are large compared to the average magnitude of the elevation changes observed in the period from 1987 to 1991. This makes it difficult to distinguish between a model that only considers further slip on the fault (dotted line in Figure 5c) and one that considers a combination of fault slip (in 1983-87) and lower crustal flow (in 1983-91) (solid line). This second model assumed 0.5 m of further slip (occurring only during the first 4 postseismic years) and lower crustal flow based on an assumed viscosity of 3×10^{18} Pa s (continuously occurring). Recall that a model that only considered lower crustal flow required a viscosity of 1×10^{18} Pa s in order to approach matching the first 4 years of observed surface deformations. Such a model leads to predicted surface deformations much larger than those observed 8 years after the quake. A model that combines both slip and slower ductile flow can be used to reasonably match both sets (4 and 8 years) of observed postseismic surface deformation.

The geodetic data shown in Figure 5c are too noisy to conclude which of the models, slip only or slip and lower crustal flow, better fits the data. Equally important is that neither model can be discounted. More accurate geodetic measurements, such as those being made of the San Fernando Valley following the 1994 Northridge quake [e.g., *Donnellan and Lyzenga*, 1996], have the potential to distinguish the subtle differences between these mechanisms, provided that the accuracy of nontectonic subsidence estimates improves significantly.

Although currently unverifiable, it remains a possibility that lower crustal flow has an influence on stresses in the upper crust many years after the Coalinga earthquake. We therefore explore how the relaxation process may influence failure stresses as a function of time after the quake by allowing the relaxation process to transfer the coseismic load to the upper crust. For this calculation we use the combined slip and lower crustal flow model described above. Figure 6a shows the calculated coseismic Coulomb failure stresses and Figures 6c and 6e show the calculated Coulomb stress at 4 and 40 Maxwell times (10 and 100 years) after the quake. We measure time by the Maxwell time τ, as this quantity is independent of the assumed viscosity. Maxwell time is defined as $\tau = \eta/G$, where η is the viscosity (in pascal seconds) and G is the shear modulus (in pascals). In this
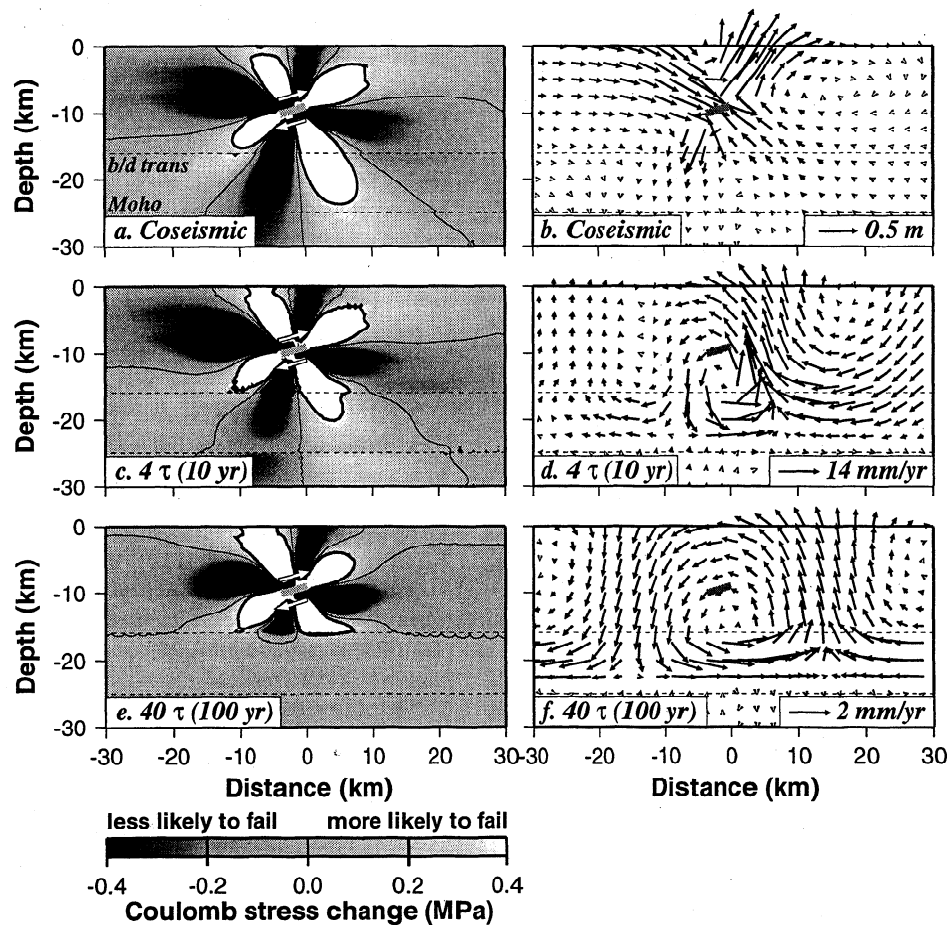

Figure 6. Calculated changes in Coulomb stress (μ'=0) and displacement and velocity vectors following the 1983 Coalinga earthquake: (a) coseismic Coulomb stress, (b) coseismic displacement, (c) Coulomb stress 4 Maxwell times after quake, (d) velocity vectors 4 Maxwell times after quake, (e) Coulomb stress after 40 Maxwell times, and (f) velocity vectors after 40 Maxwell times. In this model one Maxwell time equals ~2.5 years. Bold contour line is 0.4 MPa. Thin contour line is 0 MPa. Abbreviation b/d trans is brittle/ductile transition, and Moho indicates Moho discontinuity.
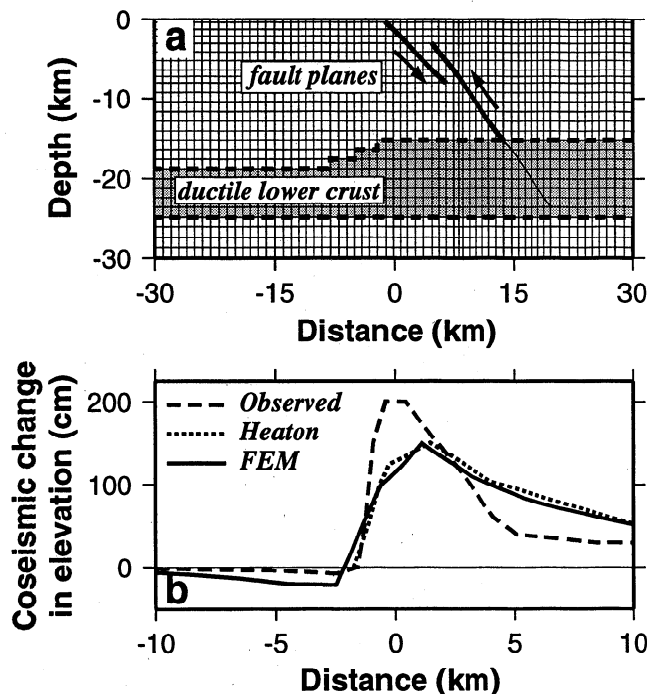
Figure 7. (a) Central portion of the 2-D finite element model used to study the 1971 San Fernando earthquake. The 2-D cross section is shown in map view as the dashed white line in Figure 1. The full model is 300 km long and 60 km deep. The earthquake occurred on two fault planes as shown [Heaton, 1982]. The model shown considers a ductile lower crust sandwiched between much stronger upper crust and upper mantle. The geometry of the brittle/ductile transition (b/d) is estimated based on the maximum depth of aftershocks [Mori et al., 1995] of the San Fernando and Northridge quakes. (b) Observed [Morrison, 1973; Savage et al., 1975; Castle et al., 1975] and calculated surface elevation changes based on Heaton [1982] and this study (FEM) for the 1971 San Fernando earthquake.

particular model, with an assumed viscosity of 3×10^{18} Pa s, 1 Maxwell time equals about 2.5 years. Thus 4τ corresponds to 10 years. If we had assumed a viscosity of 6×10^{18} Pa s (double the previous assumption), then the stress pattern predicted for 4τ (Figure 6c) would have occurred after 20 years instead of 10. The corresponding displacement and velocity profiles are shown on the right-hand side of Figure 6. Note the decreasing scale of maximum velocity shown in the bottom right-hand corner of Figures 6d and 6f. Coseismic displacement (Figure 6b) is predicted to concentrate around the original fault, while the early postseismic deformation (Figure 6d) is predicted to concentrate in the region where Coulomb stress changes in the ductile lower crust are highest. As the lower crust relaxes, the wavelength of the deformation pattern broadens (Figure 6f).

The overall pattern of calculated Coulomb stresses in the upper crust of the Coalinga region does not appear to be influenced by relaxation of the lower crust. The assumed friction coefficient does not significantly alter this result. The Coalinga case study provides an important comparison to the San Fernando case study, in which lower crustal relaxation does have a pronounced influence on calculated stresses in the upper crust.

3.2. Surface-Cutting Fault: 1971 San Fernando Quake

3.2.1. Model assumptions. The 1971 M_w=6.7 San Fernando earthquake, which occurred in the southwestern San Gabriel

Mountains, in the central Transverse Range of southern California (Figure 1), was chosen as a case study of a surface-cutting fault. The east trend of the Transverse Range results from north-south compression, attributed to convergence between the "big bend" of the San Andreas fault north of the San Gabriel Mountains and motion of the Pacific plate [Wentworth and Yerkes, 1971]. Stein et al. [1994] used a principal compressional axis for the region of N16°E in their calculations. This represents an average value based on small earthquake focal mechanisms [Gephart and Forsyth, 1984; Jones, 1988; Hauksson, 1990; Hauksson and Jones, 1991] and borehole breakouts [Mount and Suppe, 1992]. We follow this assumption and use a two-dimensional cross section that passes through the epicenter of the San Fernando main shock at this orientation as shown by the dashed line in Figure 1. The central portion of the mesh of the finite element model is shown in Figure 7a. The full model is 300 km long and extends to a depth of 60 km. The bottom boundary is fixed vertically and horizontally, and unless otherwise stated, the side boundaries are fixed horizontally. Analysis has determined that these boundary conditions do not influence model results. Slip associated with the San Fernando earthquake is inferred to have occurred on two thrust faults inclined to the north (Figure 7) [Heaton, 1982].

Elastic properties of the San Fernando model are based on the P wave velocity structure model of Kanamori and Hadley [1975], which contain no lateral variations across the San Fernando Basin. Although more recent velocity inversions show 6% lateral variations to exist [e.g., Vidale and Helmberger, 1988; Zhao and Kanamori, 1995], such variations were not considered in the finite element model because lateral density variations along the cross section of the model are not yet well constrained and because variations of this magnitude do not significantly influence the results of the present analysis. Density variations with depth are based on well log data in the region [Duke et al., 1971]. Velocity and density variations with depth along with the corresponding elastic modulus (equation (5)) are listed in Table 2. The finite element model for the San Fernando earthquake has a ductile lower crust sandwiched between an elastic upper crust and an elastic upper mantle (Figure 7a). The brittle/ductile transition is based on the maximum depth of aftershocks following the San Fernando and Northridge quakes (Figure 1b). This places the brittle/ductile transition at a depth of ~15.5-18.5 km in the study area.

3.2.2. Coseismic changes. The observed coseismic changes in elevation associated with the San Fernando quake are shown in Figure 7b. The coseismic profile was not based on a particular leveling line but rather was extracted from a contour map of elevation change assembled by Castle et al. [1975] based on an array of bench marks [Morrison, 1973; Savage et al., 1975]. The composite profile is coplanar with our model cross section.

Table 2. Elastic Properties for the San Fernando Model

Depth, km	V_P, km s^{-1}	ρ, kg m^{-3}	E, MPa	ν
0-4	5.5	2250	5.6×10^4	0.25
4-10	6.3	2500	8.2×10^4	0.25
10-15	6.3	2750	9.0×10^4	0.25
15-20	6.5	2800	9.8×10^4	0.25
20-25	6.5	3000	1.1×10^5	0.25
25-50	8.0	3250	1.7×10^5	0.25

Value V_P is the P wave velocity; ρ is the density; E is Young's modulus; ν is Poisson's ratio.

Similarly, the *Heaton* [1982] results shown in Figure 7b are taken from a cross section of a contour map of elevation changes calculated by *Heaton* [1982] based on a two fault plane model. Our finite element model is based on the same slip distribution and fault geometry used by *Heaton* [1982] and thus leads to very similar results for calculated coseismic elevation changes (Figure 7b). Both the finite element model and *Heaton*'s [1982] calculated displacements decay with distance from the fault less quickly than the observed measurements, and the maximum displacement of the calculations is smaller than that observed. *Heaton* [1982] suggests that these problems could be solved by concentrating more of the slip at shallow depth on the upper fault. *Heaton* [1982], however, concluded that the slip distribution used in his calculation provides the best overall solution for the combined observations of strong ground motions, long-period teleseismic body waves, and surface deformations.

Coseismic Coulomb stress changes associated with the San Fernando earthquake are best understood by considering the contribution of each fault plane first separately (Figures 8a and 8b) and then together (Figure 8c). Figure 8 represents end-member models of zero apparent friction. The first 4 months of aftershocks that occurred within 2 km of the modeled cross section are overlaid on the calculated stress changes caused by the earthquake (Figure 8c). Such a narrow swath of aftershocks is chosen to avoid aftershocks that occur as a result of end effects. Slip on the lower fault acts to diminish the large stress drop of the upper fault. The result is a more moderate increase in Coulomb stress along the base of the upper crust. This may help explain why we observe few aftershocks on the antithetic plane of San Fernando compared to that of Coalinga. The paucity of aftershocks might also be attributed to a poor catalog of $M_w<2$ aftershocks available for 1971 seismicity.

Figure 8d shows the calculated coseismic (slip on both faults) Coulomb stress change based on a model with a high apparent coefficient of friction of $\mu'=0.8$. The higher friction leads to higher calculated coseismic Coulomb stresses in the antithetic region. Because of uncertainties in *Heaton*'s [1982] two-fault plane solution, we also calculated coseismic Coulomb stress changes associated with a continuous fault plane bent at its center [*Langston*, 1978; *Heaton and Helmberger*, 1979]. This change in fault configuration caused moderate differences in the calculated coseismic and postseismic stress results but did not qualitatively influence conclusions. For brevity, we constrain our discussion of results to the two fault plane configuration of *Heaton* [1982].

3.2.3. Postseismic changes caused by ductile flows in lower crust.
We considered several mechanisms as potential causes of postseismic changes in Coulomb stress in the years after the 1971 San Fernando earthquake: flow within a ductile lower crust, flow within a ductile upper mantle, further slip on the original fault planes, and slip downdip of the original fault planes. If postseismic deformation occurs because of creep on the original fault planes, the postseismic change in stress would have a similar pattern to that calculated for coseismic changes (Figures 8c and 8d). The magnitude of stress change would be proportional to the amount of aseismic creep. However, other mechanisms of postseismic deformation would cause postseismic Coulomb stress changes that differ from the coseismic pattern.

Figure 9 shows the calculated changes in Coulomb stress caused by the San Fernando quake and corresponding displacement and velocity profiles at four subsequent time steps based on a model with a ductile lower crust. Unlike Coalinga, observed postseismic surface deformations are not available for the San Fernando modeled cross section. Thus we cannot use
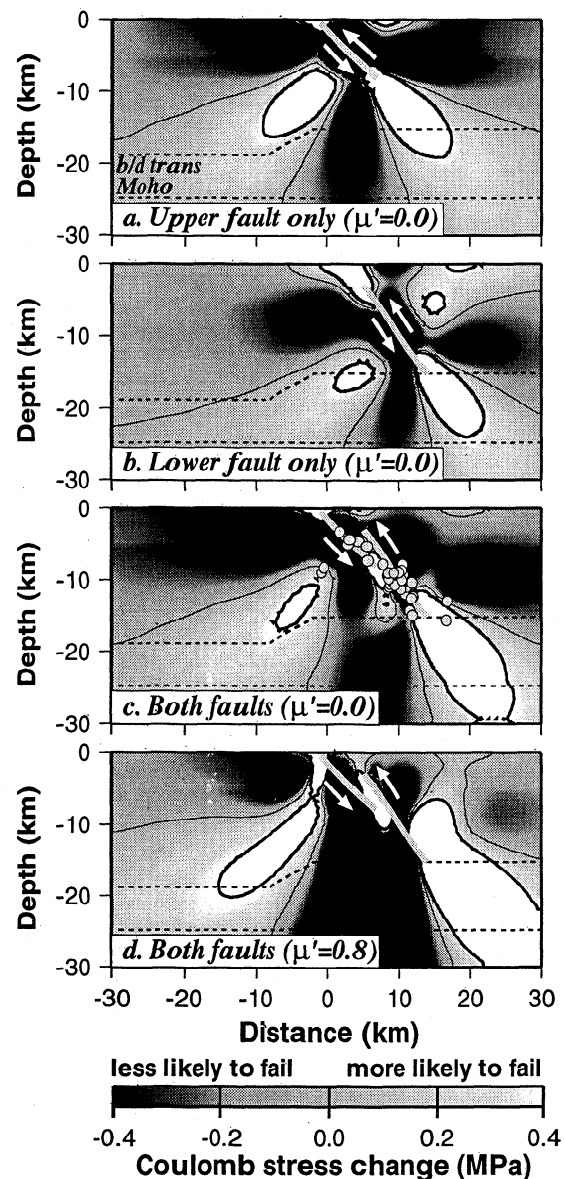

Figure 8. Predicted coseismic Coulomb stress changes ($\mu'=0$) due to the 1971 San Fernando earthquake based on slip on (a) only the upper fault, (b) only the lower fault, and (c) both faults. (d) Same as Figure 8c but for an apparent coefficient of friction of $\mu'=0.8$. The first 4 months of aftershocks within 2 km of the modeled cross section are shown in Figure 8c. Bold contour line is 0.4 MPa. Thin contour line is 0 MPa. Abbreviation b/d trans is brittle/ductile transition, and Moho indicates Moho discontinuity.

geodetic data to constrain the timing (in years) of the predicted stress and velocity changes depicted in Figure 9. For the San Fernando case study we assume a lower crustal viscosity of 10^{19} Pa s. This value is a median estimate for lower crustal viscosity based on experimental flow laws [e.g., *Kirby and Kronenberg*, 1987; *Wilks and Carter*, 1990]. The value of 3×10^{18} Pa s is on the lower side of crustal viscosities inferred from the experimental studies but is necessary to match the Coalinga geodetic data. Recall that the assumed viscosity affects only the timing of events in years but not the timing in terms of Maxwell time.

An increase in Coulomb stress is predicted in the antithetic region of San Fernando along the base of the brittle upper crust.
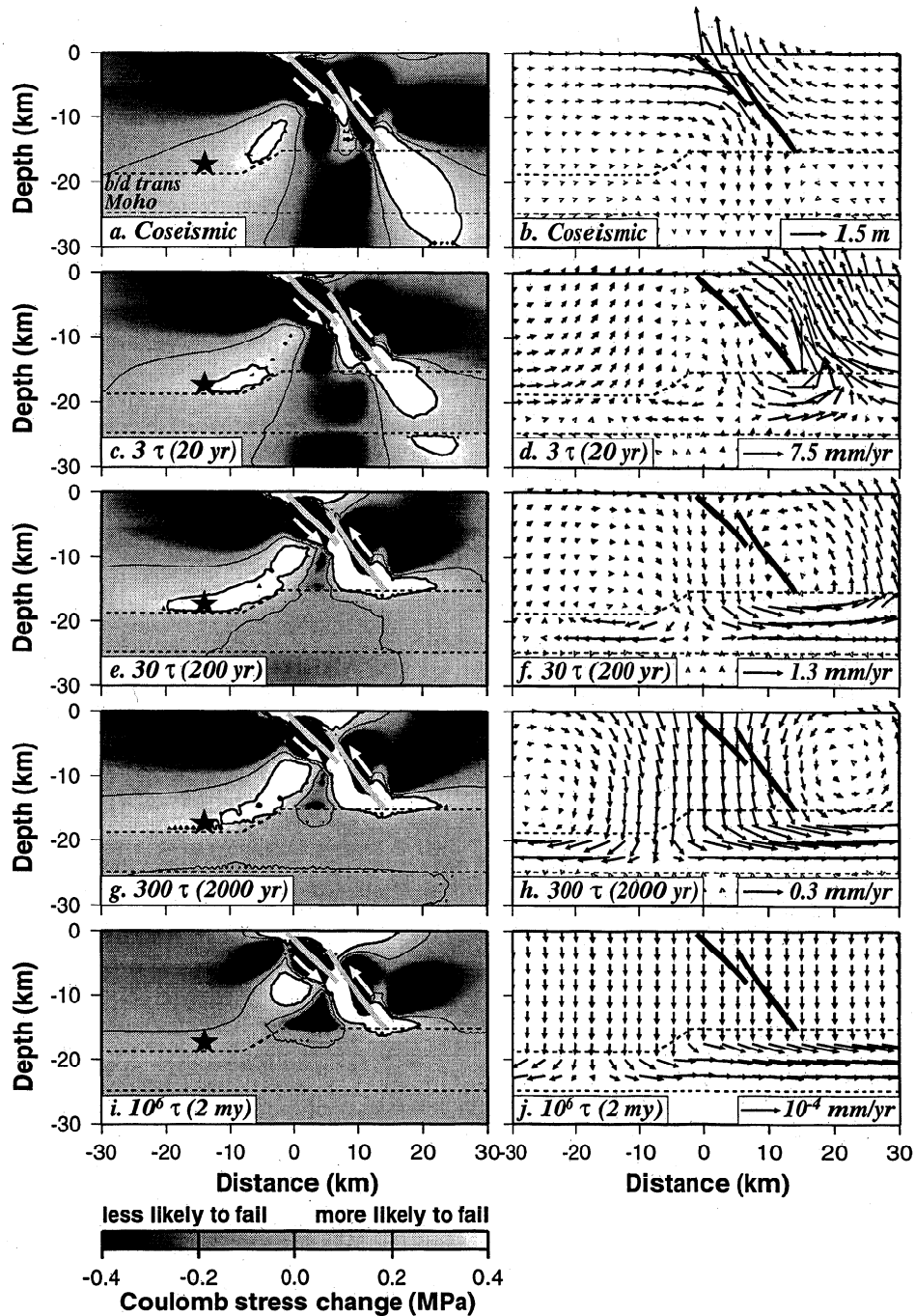
Figure 9. (left) Calculated change in Coulomb stress associated with the 1971 San Fernando earthquake (μ'=0) based on the relaxation of a ductile lower crust: (a) coseismic and postseismically after (c) 3, (e) 30, (g) 300, and (i) 1 million Maxwell times. (right) Corresponding velocity vectors: (b) coseismic (displacement) and postseismically after (d) 3, (f) 30, (h) 300, and (j) 1 million Maxwell times. Note that velocity scales decrease with time. In this model one Maxwell time equals ~6.7 years. The star is a reference location for Figure 10. Bold contour line is 0.4 MPa. Thin contour line is 0 MPa. Abbreviation b/d trans is brittle/ductile transition, and Moho indicates Moho discontinuity.

This increase in stress reaches a maximum after about 30τ (Figure 9e) and then slowly diminishes as steady state is approached (Figure 9i). The buildup in Coulomb stress in the San Fernando antithetic region is a direct result of stress being transferred from the lower to the upper crust. This is shown in the correspondence between Coulomb stress increases above the brittle/ductile transition and Coulomb stress decreases below the transition as a function of time (Figure 10a).

The influence of varying viscosity on the timing of Coulomb stress change (μ'=0) is shown in Figure 10b. If the lower viscosity were as low as 10^{18} Pa s, Coulomb stresses are predicted to be triple along the base of the upper crust in about 15 years after the San Fernando quake, although the Coalinga results did not support such a low viscosity. If the lower crustal viscosity is of the order of 10^{20} Pa s, ductile relaxation is predicted to occur on a timescale of hundreds of years. In this
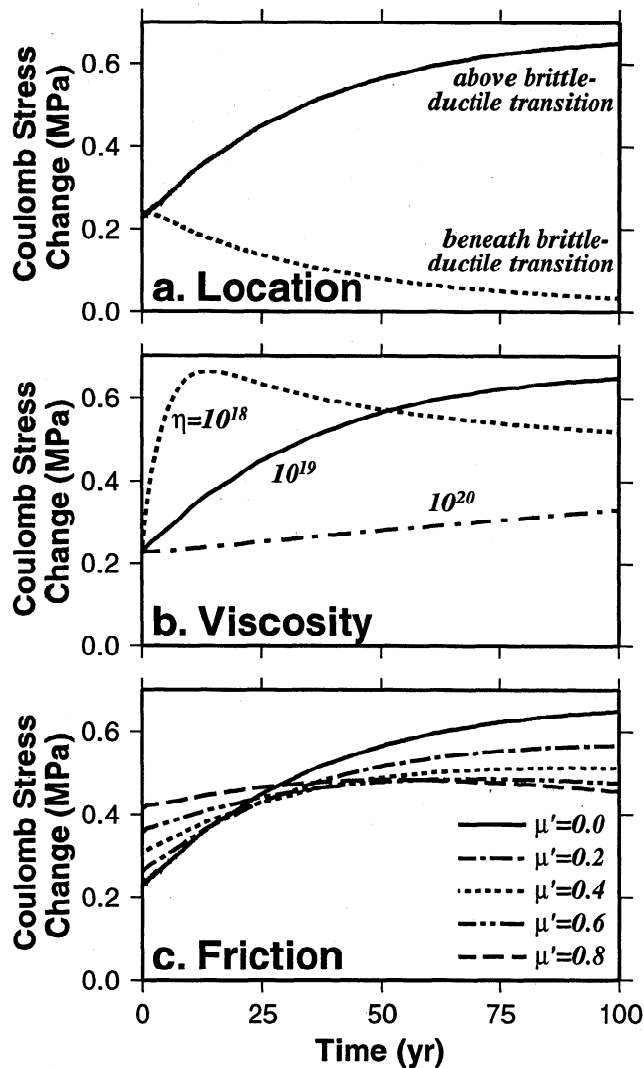
Figure 10. Calculated Coulomb stress change as a function of (a) location, (b) lower crustal viscosity, and (c) apparent coefficient of friction. The location of the "above" curve (solid curve) in Figure 10a is shown as a star in Figure 9. This same location is used for all curves in Figures 10b and 10c. In Figures 10a and 10b the apparent coefficient of friction is $\mu'=0$. In Figures 10a and 10c the lower crustal viscosity is modeled as 10^{19} Pa s.

later case, ductile relaxation would not be a likely candidate mechanism to explain faults that may have been influenced by nearby quakes in a time frame of decades.

The magnitude of calculated Coulomb stress increase in the antithetic region of San Fernando is strongly influenced by the apparent coefficient of friction assumed (Figure 10c). A low apparent friction value leads to a relatively low calculated coseismic (t=0) Coulomb stress change but with a high rate of postseismic increase. In the end-member model of no apparent friction the calculated Coulomb stress at the base of the upper crust almost doubles (from 0.23 MPa to 0.42 MPa) after 20 years of crustal relaxation following the San Fernando quake. In contrast, the models of high apparent friction lead to relatively high coseismic Coulomb stress changes (Figure 8d) and low rate of postseismic increases. Model results suggest that if enough time passes (about 50 years based on an assumed viscosity of 10^{18} Pa s), this high stress will actually diminish in the presence of a ductile lower crust. The true level of friction in the crust is

not well constrained and may be highly variable in a nonhomogeneous crust and change with time as pore pressures vary.

3.2.4. Postseismic changes caused by ductile flows in upper mantle. *Zandt and Carrigan* [1993] suggest that a small-scale convective instability beneath California may have produced a low viscosity upper mantle of the order of 1×10^{18} to 5×10^{19} Pa s. For comparison to the ductile lower crust model we develop a model with an upper mantle viscosity of 10^{19} Pa s (lower crust kept elastic). Figure 11a shows the calculated Coulomb stress change after 20 years of upper mantle relaxation following the San Fernando quake. As with a ductile lower crust (Figure 9c), a ductile upper mantle leads to an increase in Coulomb stress in the antithetic region (Figure 11a). The stress increase due to upper mantle flow is predicted to concentrate above the step in the brittle-ductile transition, not quite as far west as the ductile lower crust model. A model that considered both a ductile lower crust and upper mantle did not produce higher stress increases along the base of the upper crust when compared to the model with only a ductile lower crust.

3.2.5. Postseismic changes caused by aseismic slips on fault planes. In a study of subduction zone earthquakes, *Thatcher and Rundle* [1984] suggest the existence of a transition zone between lithosphere and asthenosphere whose behavior is brittle elastic in the short term and ductile for longer-term deformation. The crustal analogy would be for a fault in the upper crust to extend downdip into the ductile lower crust, with slip on the downdip section occurring aseismically within a few years of the coseismic event. We explored the consequences of downdip slip following the San Fernando earthquake by applying the average coseismic slip distribution of the lower fault to a
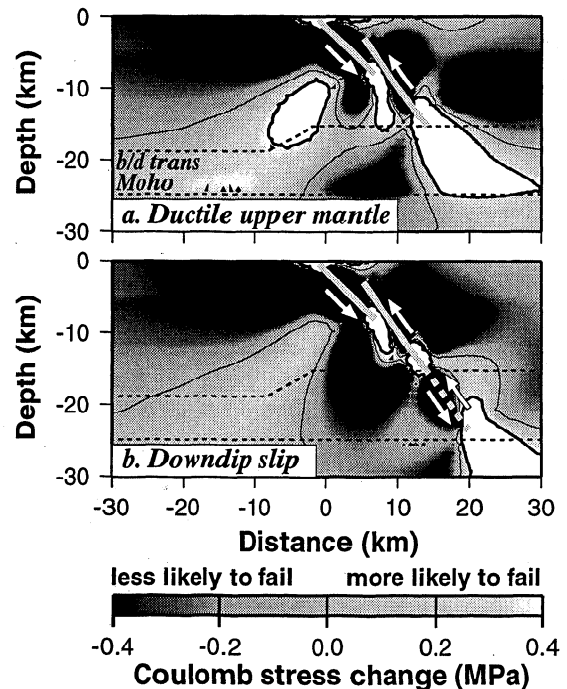

Figure 11. (a) Calculated postseismic change in Coulomb stress ($\mu'=0$.) 20 years after the San Fernando earthquake based on a model with (a) a ductile upper mantle (10^{19} Pa s) and (b) aseismic slip on a downdip section of the lower fault (light shaded dashed line). Bold contour line is 0.4 MPa. Thin contour line is 0 MPa. Abbreviation b/d trans is brittle/ductile transition, and Moho indicates Moho discontinuity.

downdip extension. This extension of the lower fault can be seen in the finite element mesh in Figure 7a. In the antithetic region of San Fernando it had been previously noted that the lower fault negated much of the coseismic Coulomb stress increase caused by the upper fault. Figure 11b suggests that extending slip downdip of the lower fault in the years following the San Fernando quake would have the effect of more completely neutralizing this stress increase. This is completely opposite to the effect of ductile flow in the lower crust or upper mantle, which serves to enhance Coulomb stress increases along the base of the upper crust.

The wavelength of the predicted postseismic surface deformation caused by the various models is strongly influenced by the depth of each corresponding mechanism (Figure 12). Aseismic slip on the original fault planes following the quake should produce a sharp postseismic displacement at the surface since the upper fault is very shallow. Models with slip on a downdip extension of the lower fault and lower crustal flow both predict longer wavelength surface deformations as both mechanisms take place in the lower crust. A ductile upper mantle would lead to the broadest surface deformations. The differences between surface deformations caused by further slip on the fault compared to a ductile lower crust (or downdip slip) are larger than those predicted in the Coalinga case, in which the Coalinga fault did not come close to the surface. As a result, postseismic geodetic data of the San Fernando quake may be used to more readily to distinguish between the models. The critical location to make a meaningful postseismic geodetic measurement would be at about 7 km north of the San Fernando epicenter (distance of +20 km in Figure 12), well within the San Gabriel mountains (See Figure 1). There are no published data regarding postseismic changes in surface elevation following the San Fernando quake. Some geodetic surveys have been conducted in the San Fernando valley in the 1980s, but none come close enough to the modeled 2-D cross section to be useful in this study. However, existing data and more accurate measurements in the future should be useful to constrain 3-D models.

3.3. Significance of Fault Dip and Depth of the Brittle/Ductile Transition

The antithetic region of high Coulomb stress at the base of the upper crust is calculated to expand laterally because of lower crustal flow following the San Fernando quake (Figures 9 and 11a) but not significantly following the Coalinga case (Figure 6). The primary factor responsible for this result is the difference in the respective fault dips and therefore the orientation of the antithetic region. Results in Figure 13 show that shallow dipping faults, such as Coalinga, lead to a steeply dipping coseismic antithetic lobe (Figure 13a) that does not expand laterally upon postseismic deformation (Figure 13b). Moderately dipping thrust faults such as San Fernando, however, lead to an antithetic region of increased coseismic Coulomb stress (Figure 13c) which grows and expands laterally upon relaxation of the lower crust (Figure 13d). Finally, a steeply dipping thrust fault does not lead to an increase of laterally expanding region of stress increase (Figures 13e and 13f), suggesting that moderate dipping faults (~45°) represent the ideal configuration for postseismic lateral expansion of an antithetic lobe of Coulomb stress increase along the base of the upper crust.

In addition to the dip angle the placement of a thrust fault relative to the brittle/ductile transition is also an important factor in determining the influence of lower ductile relaxation on stress changes. The deep thrust fault of Figure 13g leads to a region of
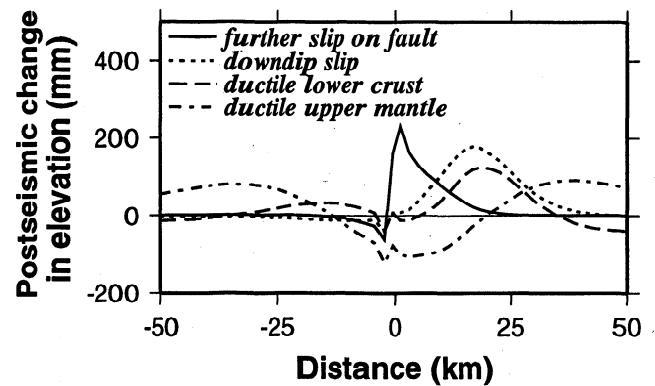

Figure 12. Calculated changes in surface elevation for various postseismic mechanisms following the San Fernando earthquake. The model that considers further slip on the fault uses an addition of 15% of the coseismic slip. The downdip slip model uses the average coseismic slip of the lower fault. The ductile models consider 20 years of relaxation after the San Fernando quake based on viscosities of 10^{19} Pa s.

coseismic Coulomb stress increase that mostly lies beneath the brittle/ductile transition. As a result, relaxation of the lower crust dissipates most of this antithetic region of high stress and, despite the moderate dip angle, does not lead to a significant lateral expansion at the base of the upper crust (Figure 13h). Therefore lateral expansion of high Coulomb stress changes require that the bottom of the thrust fault not be too close to the brittle/ductile transition such that there exists a corridor for expansion. Alternatively, a thrust fault that terminates at the brittle/ductile transition can lead to the lateral expansion of high Coulomb stress along the base of the upper crust if a neighboring region is inferred to have a deeper Moho. Such a situation is inferred to exist in the San Fernando case study where aftershocks following the Northridge quake suggest a deeper Moho to the southwest of the San Fernando fault planes (Figure 1).

3.4. Non-Newtonian Experimental Flow Laws

Assuming a Newtonian viscosity for the lower crust that does not vary with depth is likely an oversimplification of the true flow characteristics of crustal rocks. More realistic flow characteristics are usually determined by triaxial compression tests that measure the relationship between an applied differential stress σ_d and a resulting flow (strain) rate $\dot{\varepsilon}$, as a function of rock type, temperature, pressure, and water fugacity. The flow stress data are often fit with a power law of the form,

$$\dot{\varepsilon} = A \, \sigma^n \exp(Q/RT) \tag{6}$$

where A is the preexponential constant, n is the power law, Q is the activation energy, R is the universal gas constant, and T is the Kelvin temperature [e.g., *Kirby and Kronenberg*, 1987; *Carter and Tsenn*, 1987].

Because the rheology of the lower crust beneath the San Fernando Valley is not well known, we explored a variety of flow laws in an effort to deduce what rheologic parameters may support a timely postseismic transfer of stress. Rock types include the following: (1) Dry quartz aggregates are considered. Quartz is of special importance to crustal flow characteristics because of its abundance in the middle crust where it frequently encompasses the load-supporting framework of grains in the rock, and many microstructural studies of naturally deformed rocks show quartz grains to be the most deformed [*Rutter and Brodie*, 1992]. (2) Wet quartz aggregates are considered.
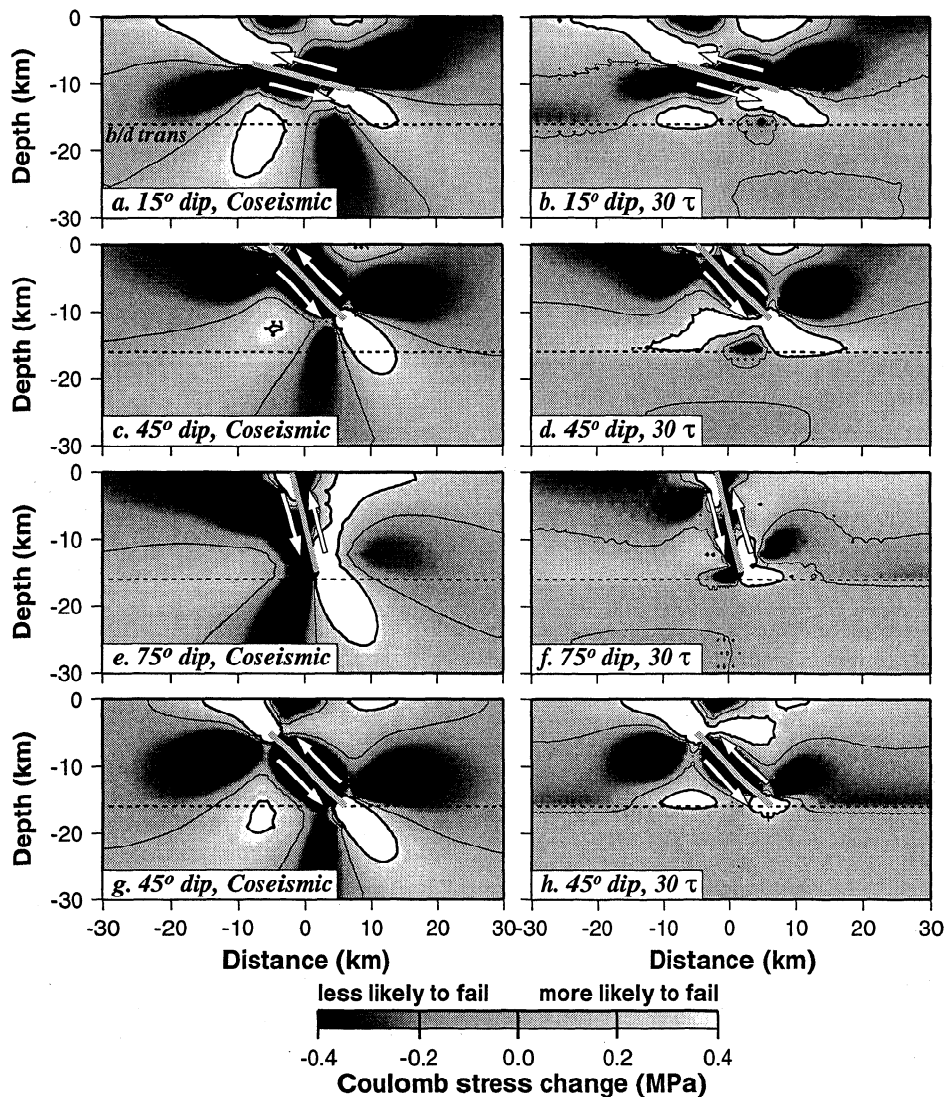
Figure 13. Calculated changes in (left) coseismic and (right) postseismic Coulomb stress changes (μ'=0.) associated with generic thrust faults with dip angles of (a) and (b) 15°, (c) and (d) 45°, (e) and (f) 75°, and (g) and (h) 45°. Postseismic stresses are based on the relaxation of a viscous lower crust after 30 Maxwell times (~240 years). All faults have identical length and slip distributions. The fault in Figures 13g and 13h has the same dip as that in Figures 13c and 13d but is located 5 km deeper. Bold contour line is 0.4 MPa. Thin contour line is 0 MPa. Abbreviation b/d trans is brittle/ductile transition.

Laboratory experiments show that most rocks experience significant hydraulic weakening when exposed to water. There is ample evidence to suggest that crustal rheologies in seismogenic zones are wet [e.g., *Brace*, 1972; *Nekut et al.*, 1977; *Brace*, 1980]. (3) Dry feldspar aggregates are considered. Feldspar rheology is likely to be of significant importance in the lower continental crust because of its volumetric importance in metabasic and dioritic rocks in which quartz does not form the principal load bearing framework [*Rutter and Brodie*, 1992]. As with quartz, feldspar aggregates are significantly affected by hydraulic weakening [*Tullis and Yund*, 1980; 1985], but the data had too much scatter from which to determine a flow law. (4) Dry and wet granite are considered. We consider granitic flow laws because of the unconstrained nature of the crustal rheology and for general comparison purposes. The steady state experimental flow laws considered in this analysis are summarized in Table 3.

We are not aware of heat flow measurements that have been taken in the San Fernando valley, but the surrounding region suggests a regional heat flow of approximately 70 +/- 10 mW m^{-2} [*Lachenbruch and Sass*, 1980]. Temperature is assumed constant in time and varies with depth according to

$$T = T_s + q_m \, (z/k) + (q_s - q_m) \, (h_r/k) \, [1 - \exp(-z/h_r)] \qquad (7)$$

where T_s is surface temperature, q_s is surface heat flux, q_m is the mantle heat flux, h_r is the characteristic length scale for the decrease of crustal radiogenic element concentration with depth, k is the thermal conductivity, and z is the depth [*Turcotte and Schubert*, 1982]. We used $T_s = 10°C$, $q_s = 58$ mW m^{-2} [*Lachenbruch and Sass*, 1980], $k = 2.5$ W m^{-1} K^{-1} [*Lachenbruch and Sass*, 1980], $q_m = 30$ mW m^{-2}, and $h_r = 10$ km [*Turcotte and Schubert*, 1982].

For purposes of comparison, we calculated the effective viscosity for each flow law as a function of depth (temperature

Table 3. Steady State Flow Parameters for Crustal Rocks

Curve*	Material	A, MPa^{-n} s^{-1}	n	Q, kJ mol^{-1}	Reference[†]
1	Black Hills quartzite (dry)	1.10×10^{-4}	4.0	223	1
2	Simpson quartzite (dry)	1.16×10^{-7}	2.7	134	2
3	Heavitree quartzite (dry)	5.00×10^{-6}	3.2	220	3
4	Heavitree quartzite (dry)	3.10×10^{-4}	2.3	171	4
5	Heavitree quartzite (dry)	9.90×10^{-6}	2.4	163	4
6	Simpson quartzite (wet)	5.05×10^{-6}	2.6	145	2
7	Heavitree quartzite (wet)	2.18×10^{-6}	2.7	120	3
8	Heavitree quartzite (wet)	5.26×10^{-3}	1.4	146	4
9	Heavitree quartzite (wet)	2.91×10^{-3}	1.8	151	4
10	Heavitree quartzite (wet)	4.00×10^{-10}	4.0	135	5
11	Hale albite (dry)	2.34×10^{-6}	3.9	234	6
12	Enfield aplite (dry)	2.34×10^{-6}	3.9	234	6
13	Westerly granite (dry)	2.00×10^{-6}	3.3	186	7
14	Westerly granite (wet)	2.00×10^{-4}	1.9	140	7

*Number corresponding to curves in Figure 14.

[†]References are as follows: 1, *Gleason and Tullis* [1995]; 2, *Koch et al.* [1989]; 3, *Kronenberg and Tullis* [1984]; 4, *Jaoul et al* [1984]; 5, *Paterson and Luan* [1990]; 6, *Shelton and Tullis* (1981); 7, *Hansen and Carter* [1983].

Value A is the preexponential constant; n is the power law; Q is the activation energy.

dependent) by assuming a uniform strain rate. The compressive strain rate across the San Fernando valley is estimated to be approximately 7.0×10^{-15} s^{-1} (0.22 μstrain yr^{-1}) [*Shen et al.*, 1996b] and approximately 4.7×10^{-15} s^{-1} (0.15 μstrain yr^{-1}) across the central Transverse Range [*Lisowski et al.*, 1991]. We used a median value of 6.0×10^{-15} s^{-1} (0.19 μstrain yr^{-1}) in our calculations. The effective viscosities for dry and wet flow laws are shown in Figures 14a and 14b, respectively. The wide scatter of viscosities reflects both large variations in crustal rock types as well as variations in experimental procedures and test conditions. The scatter seen in the wet rheologies is larger than that seen with the dry rheologies because of the strong sensitivity of rock strength to the presence of water. The shaded regions in Figures 14a and 14b denote the approximate viscosity range ($<10^{19}$ Pa s) required for a timely transfer of stress along the base of the upper crust based on the Newtonian study. None of the dry rheologies appear to satisfy this constraint, while several of the wet rheologies appear to be weak enough to allow timely transfer of stress. While this favors a wet rheology of the lower crust, we should not necessarily preclude dry crustal rocks as too strong for reasons including the following: (1) there are many uncertainties associated with laboratory-derived flow laws that can lead to an overestimation of crustal strength [e.g., *Tullis and Yund*, 1985; *Gleason and Tullis*, 1995]; and (2) even if the overall crustal matrix is strong, ductile deformation may be controlled by weak inclusions [*Ivins*, 1996].

3.5. Influence of a Regional Compressive Strain Rate

There are two steps in the calculation of Coulomb stresses. The first is to use the finite element model to calculate the stress tenser created by a quake. The second step is to calculate the Coulomb stress change of the quake stress tensor resolved on optimally oriented planes for secondary slips [*King et al.*, 1994]. The orientation of the optimum slip angle is based on the apparent coefficient of friction and the assumed regional compressive stress. We assumed a regional compressional stress of 10 MPa. As long as the assumed regional stress is significantly larger than the quake-induced coseismic stresses, which are of the order of 1 MPa, the actual magnitude of regional

stress is unimportant. With this procedure the regional compressional stress influences only the optimum slip angle of the secondary faults and does not significantly effect the process of ductile relaxation calculated by the finite element model.

There is reason to believe, however, that consideration of a regional compressive stress in the calculation of the stress tensor could influence the rate of ductile relaxation. It can be shown that viscosity is related to differential stress in the following manner;

$$\eta \propto (\sigma_r + \sigma_{co})^{1-n} \tag{8}$$

where η is viscosity, σ_r is regional differential stress, σ_{co} is coseismic differential stress, and n is the power law exponent from (6). Equation (8) suggests that the presence of a regional stress field can decrease the viscosity if the flow law is non-Newtonian (n>1). We calculated this effect using the finite element model by applying an appropriate velocity to the side of the model. A velocity boundary condition creates a regional compressive strain rate, which, in turn, causes a regional compressive stress. The problem with this approach is that a regional strain rate continuously deforms elastic regions of the model thus masking stress changes caused solely by ductile flow. To avert this situation, we modeled elastic regions with an exponential flow law [e.g., *Kronenberg et al.*, 1990; *Shea and Kronenberg*, 1992; *Ibanez and Kronenberg*, 1993] that allows us to define a limiting strength (in this case 100 MPa) such that further compressive strains do not result in higher compressive stresses.

Shen et al. [1996b] used geodetic measurements to estimate a N-S compressional strain rate of approximately 7×10^{-15} s^{-1} (0.22 μstrain yr^{-1}) across the Los Angeles basin and the San Fernando valley. We applied this strain rate using an appropriate velocity
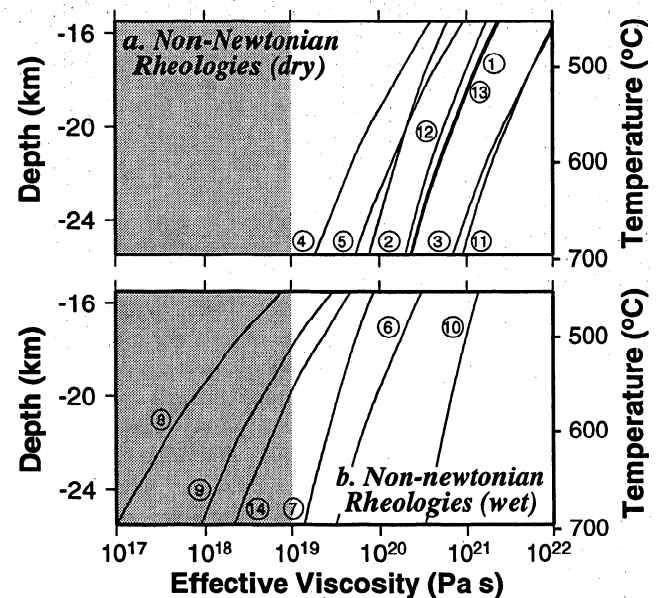

Figure 14. Effective viscosity of lower crustal rocks as a function of depth based on experimental flow laws of rocks under (a) dry and (b) wet conditions. Curve numbers correspond to flow laws listed in Table 3. Effective viscosities are calculated based on a strain rate of 6×10^{-15} s^{-1} and a surface heat flow of 70 mW m^{-2}. Shaded regions show the approximate range of effective viscosity ($<10^{19}$ Pa s) required for a significant transfer of stress from the lower to the upper crust in the time frame of 2-3 decades.

boundary condition and calculated its influence on the rate of stress transfer between a ductile lower crust and the strong upper crust. Figures 15a and 15b show the influence of the regional compressional strain rate on the calculated change in Coulomb stress along the base of the upper crust 20 years after the San Fernando quake.

Three flow law models were considered: a Newtonian (n=1) model assuming a lower crustal viscosity of 10^{19} Pa s and two non-Newtonian models (n=2 and n=4) that, in the absence of a regional compressive strain rate, lead to the same amount of stress transfer in 30 years as the Newtonian model (Figure 15a). As seen in Figure 15a, the power law exponent influences the rate of viscous relaxation. Crustal rocks with higher power law exponents tend to be weaker initially (higher rate of relaxation), then become stronger with time as the level of differential stress diminishes. This quality is amplified in the presence of a regional strain rate as shown in Figure 15b. In the presence of a regional strain rate the Newtonian (n=1) model results are unchanged compared to the model without a regional strain rate present. The two non-Newtonian models both have increased rates of stress transfer in the presence of a regional strain rate. This is potentially an important result since laboratory measurements suggest that crustal rocks behave in accordance with non-Newtonian power law exponents (Table 3).

4. Discussion

4.1. Robustness of Solution and Significance of Parameters

A significant region of model space was explored in an effort to understand which variables strongly influence the calculations. Model results suggest the following general conclusions: (1) The shear stress drop on the fault (ratio of slip to fault length) is the most important factor controlling the level of induced stresses. The larger the stress drop is, then the larger the coseismic and postseismic increases in Coulomb stress on the antithetic lobes are. (2) The fault geometry dictates the location and inclination of the antithetic lobes. Results were sensitive to a kink in the San Fernando fault plane, as opposed to a straight plane. (3) The depth of the brittle/ductile transition and Moho determines the extent of residual stress that can be translated to the base of the upper crust. The depth of the brittle/ductile transition is more important to the results than the depth of the Moho because coseismic stresses tend to be higher in the middle crust as compared to the lower crust. This effect can be somewhat offset if the lower crust relaxes much faster than the middle crust, which may occur with temperature-dependent viscosities. (4) The elastic parameters (E and v) are least influential on the results because a reduction in stiffness is approximately offset by an increase in deformation, resulting in similar predicted stress magnitudes. (5) The apparent coefficient of friction had a significant influence on stress results. The higher the assumed friction is, then the higher the coseismic Coulomb stresses are, but the lower the postseismic change in stress.

4.2. 2-D Limitations

Modeling fault rupture in two dimensions is accurate in the case of very long faults, such as those found at subduction zones. End effects associated with shorter faults may significantly influence the coseismic stress field. To examine the accuracy of the 2-D assumption in modeling faults whose along-strike length is not appreciably longer than its downdip width, we employed a 3-D boundary element code that allows comparison of stress
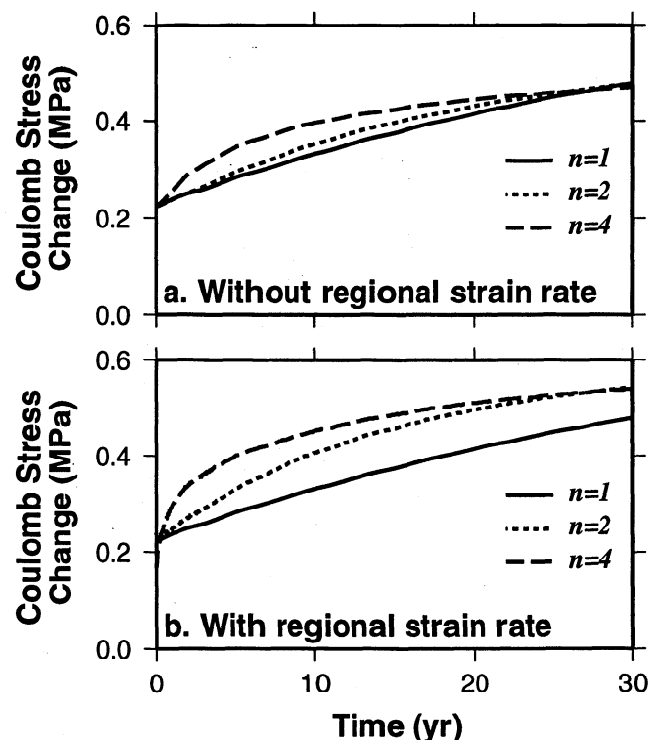

Figure 15. Calculated change in Coulomb stress at the base of the upper crust (star in Figure 9) following the San Fernando quake resulting from a ductile lower crust: (a) without the presence of a regional strain rate and (b) with a regional compressive strain rate of $7x10^{-15}$ s^{-1} (.22 μstrain yr^{-1}) across the San Fernando valley [*Shen et al.*, 1996b]. The Newtonian model (n=1) used a viscosity of 10^{19} Pa s. The non-Newtonian model (n=2) is based on the power law constants $A=10^{-4}$ Pa^{-n} s^{-1} and $Q=132$ kJ mol^{-1} (equation (6)). The non-Newtonian model (n=4) is based on the power law constants $A=10^{-4}$ Pa^{-n} s^{-1} and $Q=110$ kJ mol^{-1}.

results of faults with varying widths. The elastic half-space, 3-D boundary element code [*King et al.*, 1994] was used to model a generic blind thrust fault with a uniform slip of 1 m. We considered several models of varying along-strike fault length. Figure 16a shows the calculated coseismic stress changes associated with a fault with 15 km of along-strike length, comparable to the length of the San Fernando fault. The stresses in Figure 16 are calculated along a plane perpendicular to strike and bisecting the fault, that is, the cross section that would be assumed by a 2-D model. Figure 16b shows the results of the same fault but with an along-strike length of 1000 km. A comparison of these results suggests that modeling a fault with 15-km along-strike length as a 1000-km-long fault tends to moderately overestimate the magnitude of stresses but does not significantly influence the stress pattern along the centerline cross section. Such an approximation has less error for the Coalinga fault with its 25-km along-strike length. Figure 16c shows that the 2-D finite element calculation of the same fault results in stresses nearly identical to the 3-D boundary element model of a 1000-km-long fault.

The above calculations suggest that the 2-D assumption for faults such as San Fernando and Coalinga is probably reasonable along the centerline cross section. However, differences between 2-D and 3-D results will increase dramatically with distance away from this centerline. In addition, there is potentially a time-dependent problem associated with the fact that a plane strain
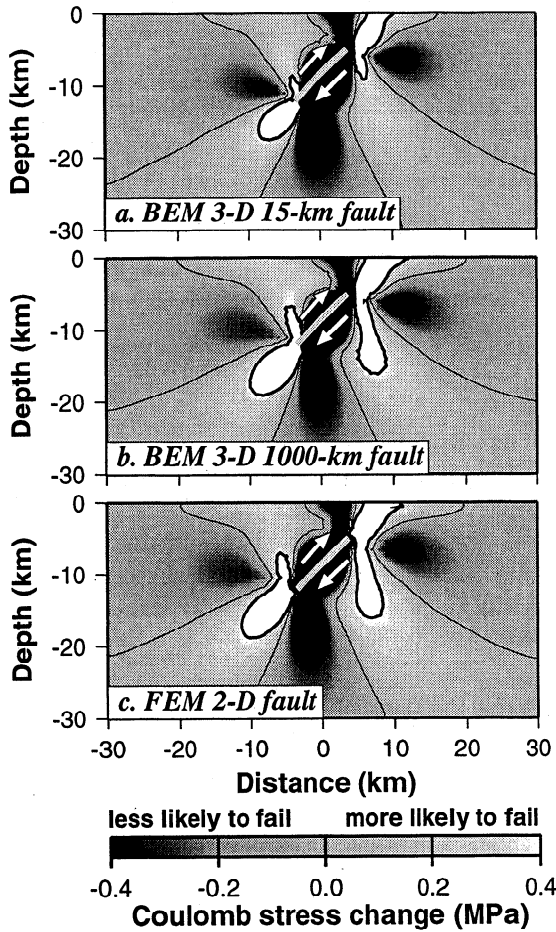
Figure 16. Calculated coseismic Coulomb stresses associated with a generic blind thrust fault based on (a) a 3-D boundary element model (BEM) of a 15-km-long fault, (b) a 3-D boundary element model of a 1000 km long fault, and (c) a 2-D finite element model (FEM) that assumes infinite fault length. Bold contour line is 0.4 MPa. Thin contour line is 0 MPa.

Furthermore, if the repeat time of a thrust fault is of the order of hundreds or even thousands of years, then the steady state solution, which occurs on a timescale of the order of millions of years, is never achieved. The path dependence of the viscoelastic solution for dipslip earthquakes is probably also true for strike-slip quakes. Thus caution should be exercised in the usage of thin-plate approximations to predict long-term stress changes.

5. Conclusions

Two-dimensional calculations using viscoelastic finite element models suggest that thrust earthquakes cause a coseismic increase in Coulomb stress along antithetic lobes normal to the slip plane. Calculations suggest that if a ductile lower crust or upper mantle flows viscously following a thrust event, relaxation may cause a transfer of stress to the upper crust. Under certain conditions this may lead to further increases and a lateral expansion of high Coulomb stresses along the base of the upper crust. The conditions under which an antithetic lobe of high Coulomb stress are favored to expand postseismically within a few decades include the following: the lower crust or upper mantle has an effective viscosity not greater than 10^{19} Pa s, the thrust fault has a moderate dip angle ($40°$-$50°$), the brittle/ductile transition is deep enough to provide a corridor at the base of the upper crust for expansion, and the crust has a low apparent coefficient of friction (<0.2). Postseismic increases in Coulomb stress within the upper crust may also be caused by aseismic creep on the original fault. Stress changes due to this mechanism are maximized with a high apparent coefficient of friction. Analysis of experimentally determined non-Newtonian flow laws suggests that wet granitic, quartz, and feldspar aggregates may yield a viscosity of the order of 10^{19} Pa s. The calculated rate of stress transfer from a viscous lower crust or upper mantle to the upper crust becomes faster with increasing values of the power law exponent and the presence of a regional compressive strain rate. Results of this 2-D analysis suggest a potentially important role of viscous flow in controlling time-dependent postseismic stress changes that warrant further investigation using 3-D viscoelastic analysis.

model does not allow viscous flow perpendicular to the modeled cross section. Nevertheless, the 2-D modeling approach is an important first step in understanding some of the fundamental properties regarding the influence of lower crustal relaxation on stress distribution following thrust earthquakes.

4.3. Comparison to Thin-Plate Solutions

In order to calculate the postseismic state of stress upon the completion of lower crustal relaxation, several previous studies have attempted to shortcut the tedium of conducting a time-dependent, viscoelastic analysis by conducting an elastic analysis in which the lower crust is modeled as an inviscid fluid beneath a thin-plate upper crust [e.g., *Stein et al.*, 1992; *King et al.*, 1994; *Stein et al.*, 1994]. Thin-plate elastic solutions calculate the long-term, steady state solution in which the lower crust has completely relaxed. As a result, the thin-plate solution is nearly identical to the steady state solution shown in Figure 9i. Unfortunately, the transient process of lower crustal relaxation is not uniform with time (Figure 9). Instead, velocity structures broaden in a nonuniform manner such that interim states of stress in certain regions of the crust, such as along the antithetic region of San Fernando, have a higher stress level early in the relaxation process compared to the long-term, steady state solution.

References

Bodin, P., and J. Gomberg, Triggering seismicity and deformation between the Landers, California, and Little Skull Mountain, Nevada, earthquakes, *Bull. Seismol. Soc. Am.*, *84*, 835-843, 1994.

Brace, W. F., Pore pressure in geophysics, in *Flow and Fracture of Rocks, Geophys. Monogr. Ser.*, vol. 16, edited by H. C. Heard et al., pp. 265-273, AGU, Washington, D. C., 1972.

Brace, W. F., Permeability of crystalline and argillaceous rocks, *Int. J. Rock Mech. Mining Sci. Geomech. Abstr.*, *17*, 241-251, 1980.

Burgmann, R., P. Segall, M. Lisowski, and J. Svarc, Postseismic strain following the 1989 Loma Prieta earthquake from GPS and leveling measurements, *J. Geophys. Res.*, *102*, 4933-4956, 1997.

Carter, N. L., and M. C. Tsenn, Flow properties of continental lithosphere, *Tectonophysics*, *136*, 27-63, 1987.

Castle, R. O., J. P. Church, M. R. Elliott, and N. L. Morrison, Vertical

crustal movements preceding and accompanying the San Fernando earthquake of February 9, 1971: A summary, *Tectonophysics, 29*, 127-140, 1975.

Donnellan, A., and G. A. Lyzenga, Northridge postseismic deformation: Inferences from continuous and campaign GPS observations (abstract), *Eos Trans. AGU, 77(46)*, Fall Meet. Suppl., F147, 1996.

Duke, C. M., J. A. Johnson, Y. Kharraz, K. W. Campbell, and N. A. Malpiede, Subsurface site conditions and geology in the San Fernando earthquake area, *Rep. UCLA-ENG-7206*, Sch. of Eng., Univ. of Calif., Los Angeles, 1971.

Eberhart-Phillips, D., Three-dimensional *P* and *S* velocity structure in the Coalinga region, California, *J. Geophys. Res., 95*, 15,343-15,363, 1990.

Ekstrom, G., R. S. Stein, J. P. Eaton, and D. Eberhart-Phillips, Seismicity and geometry of a 110-km-long blind thrust fault, 1, The 1985 Kettleman Hills, California, earthquake, *J. Geophys. Res., 97*, 4843-4864, 1992.

Fuis, G. S., and W. D. Mooney, Lithospheric structure and tectonics from seismic-reflection and other data, in *The San Andreas Fault System, California*, edited by R. E. Wallace, *U.S. Geol. Surv. Prof. Pap., 1515*, 207-238, 1990.

Gephart, J. W., and D. W. Forsyth, An improved method for determining the regional stress tensor using earthquake focal mechanism data: Application to the San Fernando earthquake sequence, *J. Geophys. Res., 89*, 9305-9320, 1984.

Gleason, G. C., and J. Tullis, A flow law for dislocation creep of quartz aggregates determined with the molten salt cell, *Tectonophysics, 247*, 1-23, 1995.

Griscom, A., and R. C. Jachens, Tectonic implications of gravity and magnetic models along east-west seismic profiles across the Great Valley near Coalinga, *in The Coalinga, California, Earthquake of May 2, 1983*, edited by M. Rymer and W. Ellsworth, *U.S. Geol. Surv. Prof. Pap., 1487*, 69-78, 1990.

Hansen, F. D., and N. L. Carter, Semibrittle creep of dry and wet Westerly granite at 1000 MPa, paper presented at 24th U.S. Symposium on Rock Mechanics, Texas A & M Univ., College Station, Tex., 1983.

Harris, R. A., and R. W. Simpson, Changes in static stress on southern California faults after the 1992 Landers earthquake, *Nature, 360*, 251-254, 1992.

Hauksson, E., Earthquakes, faulting, and stress in the Los Angeles Basin, *J. Geophys. Res., 95*, 15,365-15,394, 1990.

Hauksson, E., and L. M. Jones, The 1988 and 1990 Upland earthquakes: Left-lateral faulting adjacent to the central Transverse Ranges, *J. Geophys. Res., 96*, 8143-8165, 1991.

Heaton, T. H., The 1971 San Fernando earthquake: a double event?, *Bull. Seismol. Soc. Am., 72*, 2037-2062, 1982.

Heaton, T. H., and D. V. Helmberger, Generalized ray models of the San Fernando earthquake, *Bull. Seismol. Soc. Am., 69*, 1311-1341, 1979.

Hopson, C. A., J. M. Mattinson, and E. A. Pessagno Jr., Coast Range ophiolite, western California, in *The Geotectonic Development of California*, edited by W. G. Ernst, pp. 418-510, Prentice-Hall, Englewood Cliffs, N. J., 1981.

Ibanez, W. D., and A. K. Kronenberg, Experimental deformation of shale: Mechanical properties and microstructural indicators of mechanisms, *Int. J. Rock Mech. Min. Sci. Geomech. Abstr., 30*, 723-734, 1993.

Ivins, E. R., Transient creep of a composite lower crust, 2, A polymineralic basis for rapidly evolving postseismic deformation modes, *J. Geophys. Res., 101*, 28,005-28,028, 1996.

Jaeger, J. C., and N. G. W. Cook, *Fundamentals of Rock Mechanics*, 3rd ed., Chapman and Hall, New York, 1979.

Jaoul, O., J. Tullis, and A. Kronenberg, The effect of varying water contents on the creep behavior of Heavitree quartzite, *J. Geophys. Res., 89*, 4298-4312, 1984.

Jaume, S. C., and L. R. Sykes, Changes in state of stress on the southern San Andreas fault resulting from the California earthquake sequence of April to June 1992, *Science, 258*, 1325-1328, 1992.

Jones, L. M., Focal mechanisms and the state of stress on the San Andreas Fault in Southern California, *J. Geophys. Res., 93*, 8869-8891, 1988.

Kanamori, H., and D. Hadley, Crustal structure and temporal velocity change in southern California, *Pure Appl. Geophys., 113*, 257-280, 1975.

King, G. C. P., R. S. Stein, and J. Lin, Static stress changes and the triggering of earthquakes, *Bull. Seismol. Soc. Am., 84*, 935-953, 1994.

Kirby, S. H., and A. K. Kronenberg, Rheology of the lithosphere: Selected topics, *Rev. Geophys., 25*, 1219-1244, 1987.

Koch, P. S., J. M. Christie, A. Ord, and R. P. George Jr., Effect of water on the rheology of experimental deformed quartzite, *J. Geophys. Res., 94*, 13,975-13,996, 1989.

Kronenberg, A. K., and J. Tullis, Flow strength of quartz aggregates: Grain size and pressure effects due to hydrolytic weakening, *J. Geophys. Res., 89*, 4281-4297, 1984.

Kronenberg, A. K., S. H. Kirby, and J. Pinkston, Basal slip and mechanical anisotropy of biotite, *J. Geophys. Res., 95*, 19,257-19,278, 1990.

Lachenbruch, A. H., and J. H. Sass, Heat flow and energetics of the San Andreas fault zone, *J. Geophys. Res., 85*, 6185-6222, 1980.

Langston, C. A., The February 9, 1971, San Fernando earthquake: A study of source finiteness in teleseismic body waves, *Bull. Seismol. Soc. Am., 68*, 1-29, 1978.

Li, V. C., and J. R. Rice, Crustal deformation in great California earthquake cycles, *J. Geophys. Res., 92*, 11,533-11,551, 1987.

Lisowski, M., J. C. Savage, and W. H. Prescott, The velocity field along the San Andreas Fault in central and southern California, *J. Geophys. Res., 96*, 8369-8389, 1991.

Melosh, H. J., and A. Raefsky, The dynamic origin of subduction zone topography, *Geophys. J. R. Astro. Soc., 60*, 333-354, 1980.

Melosh, H. J., and C. A. Williams Jr., Mechanics of graben formation in crustal rocks: A finite element analysis, *J. Geophys. Res., 94*, 13,961-13,973, 1989.

Mori, J., D. J. Wald, and R. L. Wesson, Overlapping fault planes of the 1971 San Fernando and 1994 Northridge, California earthquakes, *Geophys. Res. Lett., 22*, 1033-1036, 1995.

Morrison, N. L., Vertical crustal movements determined from surveys before and after the San Fernando earthquake, in San Fernando, California, Earthquake of February 9, 1971, Geol. Geophys. Stud., vol. 3, pp. 295-324, Natl. Oceanic and Atmos. Admin., U.S. Dep. of Commer., Silver Spring, Md., 1973.

Mount, V. S., and J. Suppe, Present-day stress orientations adjacent to active strike-slip faults: California and Sumatra, *J. Geophys. Res., 97*, 11,995-12,013, 1992.

Nekut, A., J. E. P. Connerney, and A. F. Kuckes, Deep crustal electrical conductivity: Evidence for water in the lower crust, *Geophys. Res. Lett., 4*, 239-242, 1977.

Nur, A., and G. Mavko, Post-seismic viscoelastic rebound, *Science, 183*, 204-206, 1974.

Oppenheimer, D. H., P. A. Reasenberg, and R. W. Simpson, Fault plane solutions for the 1984 Morgan Hill, California, earthquake sequence: Evidence for the state of stress on Calavares fault, *J. Geophys. Res., 93*, 9007-9026, 1988.

Page, B. M., The southern Coast Ranges, in *The Geotectonic Development of California*, edited by W. G. Ernst, pp. 329-417, Prentice-Hall, Englewood Cliffs, N. J., 1981.

Paterson, M. S., and F. C. Luan, Quartz rheology under geological conditions, in *Deformation Mechanisms, Rheology and Tectonics*, edited by R. J. Knipe and E. H. Rutter, *Geol. Soc. Spec. Publ., 54*, 299-307, 1990.

Reasenberg, P. A., and R. W. Simpson, Response of regional seismicity to the static stress change produced by the Loma Prieta earthquake, *Science, 255*, 1687-1690, 1992.

Rutter, E. H., and K. H. Brodie, Rheology of the lower crust, in *Continental Lower Crust, Dev. Geotecton.*, vol 23, edited by D. M. Fountain, R. Arculus, and R. W. Kay, pp. 201-267, Elsevier, New York, 1992.

Savage, J. C., R. O. Burford, and W. T. Kinoshita, Earth movements from geodetic measurements, in *San Fernando Earthquake of 9 February 1971*, edited by G. B. Oakeshott, *Bull. Calif. Div. Mines Geol., 196*, 175-186, 1975.

Shea, W., and A. Kronenberg, Rheology and deformation mechanisms of an isotropic mica schist, *J. Geophys. Res., 97*, 15,201-15,237, 1992.

Shelton, G., and J. Tullis, Experimental flow laws for crustal rocks (abstract), *Eos Trans. AGU, 62* (17), 396, 1981.

Shen, Z., D. D. Jackson, Y. Feng, M. Cline, M. Kim, P. Fang, and Y. Bock, Postseismic deformation following the Landers earthquake, California, 28 June, 1992, *Bull. Seismol. Soc. Am., 84*, 780-791, 1994.

Shen, Z., D. D. Jackson, L. Sung, D. Potter, and B. Ge, Tectonic implications of the southern California Earthquake Center crustal deformation map (abstract), *Eos Trans. AGU, 77* (46), Fall Meet. Suppl., F148, 1996a.

Shen, Z., D. D. Jackson, and B. X. Ge, Crustal deformation across and beyond the Los Angeles basin from geodetic measurements, *J. Geophys. Res., 101*, 27,957-27,980, 1996b.

Simpson, R. W., and P. A. Reasenberg, Earthquake-induced static-stress changes on central California faults, in *The Loma Prieta, California, earthquake of October 17, 1989: Tectonic Processes and Models*, edited by R. W. Simpson, *U.S. Geol. Surv. Prof. Pap.*, F55-F89, 1994.

Stein, R. S., and G. Ekstrom, Seismicity and geometry of a 110-km-long blind thrust fault, 2, Synthesis of the 1982-1985 California earthquake sequence, *J. Geophys. Res.*, *97*, 4865-4883, 1992.

Stein, R. S., G. C. P. King, and J. Lin, Change in failure stress on the southern San Andreas Fault system caused by the 1992 magnitude = 7.4 Landers earthquake, *Science, 258*, 1328-1332, 1992.

Stein, R. S., G. C. P. King, and J. Lin, Stress triggering of the 1994 M=6.7 Northridge, California, earthquake by its predecessors, *Science, 265*, 1432-1435, 1994.

Thatcher, W., and J. B. Rundle, A viscoelastic coupling model for the cyclic deformation due to periodically repeated earthquakes at subduction zones, *J. Geophys. Res.*, *89*, 7631-7640, 1984.

Tse, S. T., and J. R. Rice, Crustal earthquake instability in relation to the depth variation of frictional slip properties, *J. Geophys. Res.*, *91*, 9452-9472, 1986.

Tullis, J., and R. A. Yund, Hydrolytic weakening of experimentally deformed Westerly granite and Hale albite rock, *J. Struct. Geol.*, *2*, 439-451, 1980.

Tullis, J., and R. A. Yund, Dynamic recrystallization of feldspar: A mechanism for ductile shear zone formation, *Geology, 13*, 238-241, 1985.

Turcotte, D. L. and G. Schubert, *Geodynamics*, 450 pp., John Wiley, New York, 1982.

Vidale, J. E., and D. V. Helmberger, Elastic finite-difference modeling of the 1971 San Fernando, California earthquake, *Bull. Seismol. Soc. Am.*, *78*, 122-141, 1988.

Wentworth, C. M., and R. F. Yerkes, Geologic setting and activity of faults in the San Fernando area, California, *U.S. Geol. Surv. Prof. Pap.*, *733*, 6-16, 1971.

Wessel, P., and W. H. F. Smith, Free software helps map and display data, *Eos Trans. AGU, 72* (44), 444, 1991.

Wilks, K. R., and N. L. Carter, Rheology of some continental lower crustal rocks, *Tectonophysics, 182*, 57-77, 1990.

Wyatt, F., D. C. Agnew, and M. Gladwin, Continuous measurements of crustal deformation for the 1992 Landers earthquake sequence, *Bull. Seismol. Soc. Am.*, *84*, 768-779, 1994.

Zandt, G., and C. R. Carrigan, Small-scale convective instability and upper mantle viscosity under California, *Science, 261*, 460-463, 1993.

Zhao, D., and H. Kanamori, The 1994 Northridge earthquake: 3-D crustal structure in the rupture zone and its relation to the aftershock locations and mechanisms, *Geophys. Res. Lett.*, *22*, 763-766, 1995.

A.M. Freed, Department of Terrestrial Magnetism, Carnegie Institution of Washington, 5241 Broad Branch Road, NW, Washington, DC 20015. (e-mail: freed@dtm.ciw.edu)

J. Lin, Department of Geology and Geophysics, Woods Hole Oceanographic Institution, Woods Hole, MA 02543. (e-mail: jlin@whoi.edu)